Original Article

Subducted oceanic slab break-off in a post-collisional setting: Constraints from petrogenesis of Late Carboniferous dykes in central West Junggar, Xinjiang, NW China

Rui Gao[1,2] , Jinke Li[1] , Andrew C. Kerr[2], Tao Wu[3] , Long Xiao[4], Guocan Wang[4] and Xinxing He[5]

[1]College of Earth Science, Chengdu University of Technology, Chengdu, China; [2]School of Earth and Environmental Sciences, Cardiff University, Cardiff, South Glamorgan, UK; [3]Ocean College, Zhejiang University, Zhoushan, China; [4]School of Earth Sciences, China University of Geosciences, Wuhan, China and [5]Geological Survey of Jiangsu Province, Nanjing, China

Abstract

Numerous Late Carboniferous – Early Permian dykes are found in West Junggar and represent an important part of the Central Asian Orogenic Belt. In this contribution, we use these dykes to assess the tectonic regime and stress state in the Late Carboniferous – Early Permian. The West Junggar dykes are mainly diorite/dioritic porphyrite with minor diabase and were formed in 324–310 Ma. They have been divided into two groups based on their orientation, petrology and geochronology. Group 1 dykes mostly comprise WNW-striking dioritic porphyrite and NE-striking diorite with minor diabase and resemble the Karamay-Baogutu sanukitoid. They were probably formed from depleted mantle at a relatively high temperature and pressure with the addition of 1–2% sediment/sedimental partial melt and 0–5% trapped oceanic crust-derived melts. Group 2 dykes are ENE-striking and are similar to sanukite in the Setouchi Volcanic Belt. These dykes were also derived from depleted mantle at a shallow depth but high temperature with the addition of 2–3.5% sediment/sedimental partial melt. Magma banding and injection folds in dykes and host granitoids indicate magma flow. Paleostress analysis reveals that both groups of dykes were formed in a tensile stress field. Their emplacement is favoured by presence of pre-existing joints or fractures in the host granitoids and strata. We conclude that large-scale asthenosphere mantle upwelling induced by trapped oceanic slab-off can explain the magmatism and significant continental crustal growth of West Junggar during Late Carboniferous to Early Permian.

1. Introduction

The Central Asian Orogenic Belt (CAOB) (also known as the Altaid Tectonic Collage) is the world's largest Palaeozoic accretionary orogen (Fig. 1). The CAOB is related to the closure of the Palaeo-Asian Ocean and represents a significant region of Phanerozoic crustal growth (Coleman, 1989; Sengör *et al.* 1993; Jahn *et al.* 2000, 2004; Windley *et al.* 2007; Wilde *et al.* 2010; Xu *et al.* 2013). It is widely accepted that the CAOB is related to the closure of the Palaeo-Asian Ocean from the Early Neoproterozoic to the Late Palaeozoic (Jahn *et al.* 2000; Chen & Jahn, 2004; Han *et al.* 2006; Windley *et al.* 2007; Xiao & Santosh, 2014). This closure involved the accretion of oceanic islands, seamounts, oceanic plateaus, island arcs, accretionary complexes, ophiolites and microcontinents to the southern margin of the Siberian Craton (Feng *et al.* 1989; Windley *et al.* 2007; Xiao *et al.* 2008, 2010; Zhang *et al.* 2021a, 2021b).

The West Junggar region, in the southwestern part of the CAOB, plays a crucial role in understanding the Palaeozoic tectonic evolution and crustal growth within the orogenic belt (Windley *et al.* 2007; Xiao *et al.* 2008; Choulet *et al.* 2012; Xu *et al.* 2013). Both lateral accretion in active continental margins and vertical underplating at the crust-mantle interface contributed to continental crustal growth in CAOB (Jahn *et al.* 2000; Windley *et al.* 2007). Voluminous Late Palaeozoic granitoids with high and positive εNd*(t)* values were intruded throughout West Junggar (Jahn *et al.* 2000; Chen & Jahn, 2004; Han *et al.* 2006) and include a range of magmatic rocks including high-Mg andesites (e.g., sanukitoids/sanukitic rocks, adakites/adakitic rocks), A- and I-type granites and Nb-enriched diorites (Chen *et al.* 2010; Yin *et al.* 2010, 2015a; Tang *et al.* 2012a, 2012b; Xu *et al.* 2013; Zhang *et al.* 2018, 2021a; Zheng *et al.* 2020). However, the tectono-magmatic setting of these Late Carboniferous to Permian magmatic rocks in West Junggar remains controversial with a range of tectonic settings and processes being proposed. These include: post-collisional (Chen & Jahn, 2004; Han *et al.* 2006; Chen *et al.* 2010; An *et al.* 2022b), mantle plume (Gao *et al.* 2014), remnant oceanic basin (Xu *et al.* 2013;
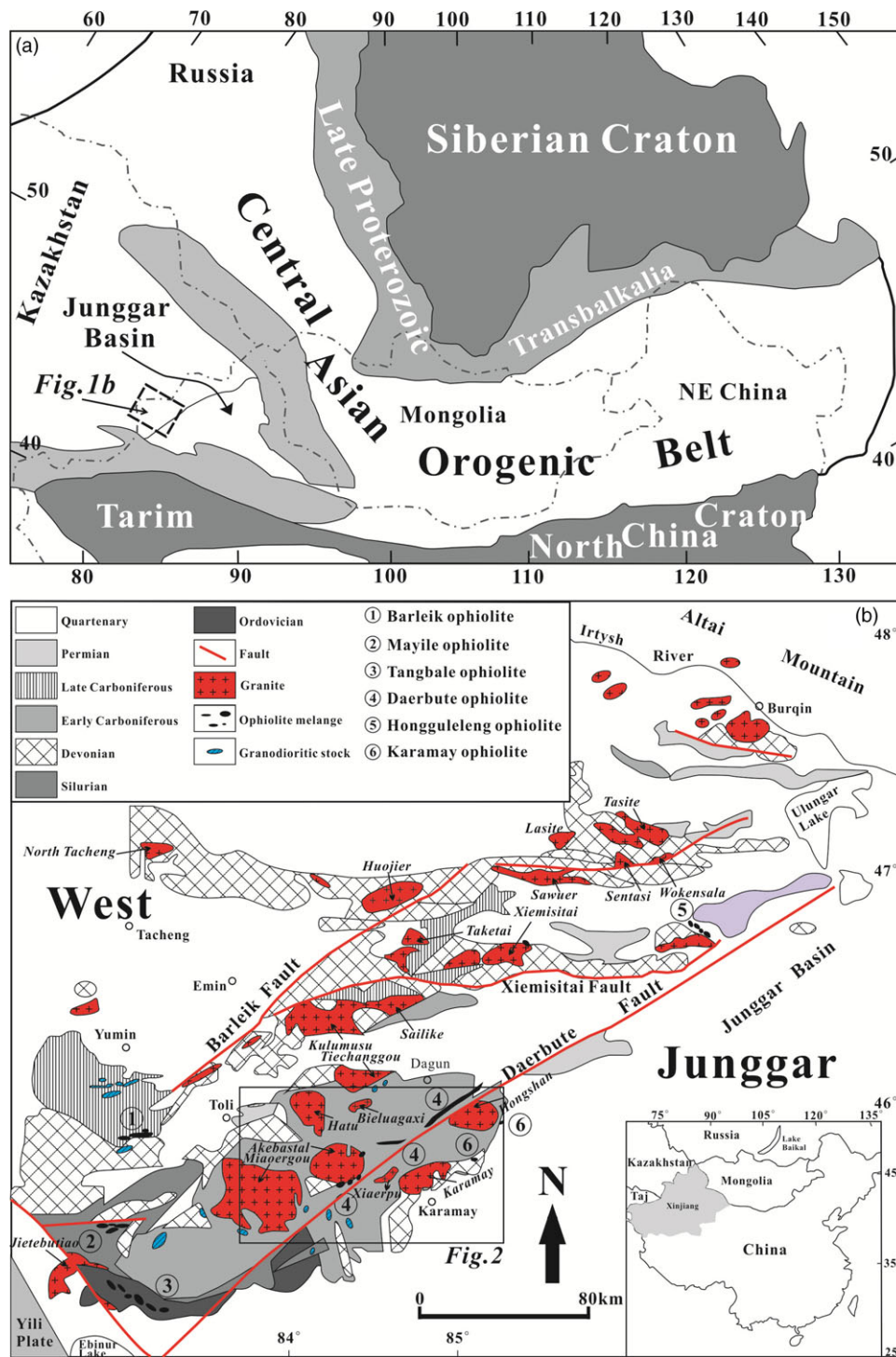
Figure 1. (Colour online) (a) Simplified tectonic map of the Central Asian Orogenic Belt (Sengör *et al.* 1993). (b) Simplified geological map of the West Junggar (modified after Feng *et al.* 1989), inset shows the position of Xinjiang in NW China.

Zhang *et al.* 2018), subduction-accretion (Xiao *et al.* 2008, 2010) and ridge subduction (Geng *et al.* 2009; Tang *et al.* 2010, 2012a, 2012b; Yin *et al.* 2013, 2015b, 2015a; Windley & Xiao, 2018) processes.

Intermediate-mafic dykes are widespread in the southern West Junggar (Fig. 1), especially in the Karamay, Xiaerpu, Bieluagaxi and Liushugou areas (Fig. 2), which provide an excellent opportunity to understand the geological evolution of the West Junggar. The dykes in West Junggar are referred to as high-magnesium andesites (HMAs) including sanukitoids and adakitic-like rocks (Yin *et al.* 2010, 2013; Duan *et al.* 2019), which are distinct from typical island arc andesites due to their elevated SiO_2, MgO and Mg# (Mg# = $Mg^{2+}/(Mg^{2+}+Fe^{2+})$), Cr and Ni contents (Tatsumi, 2001). Their geochemical and isotopic features reveal an affinity of both mantle and crust and an uncommon tectonic setting in association with subduction zones or post-collisional

Figure 2. (Colour online) (a) Geological map of the study area (modified after Ma *et al.* 2012). Positions of Fig. 2b–d are marked. (b) Simplified geological map of the Karamay and Xiaerpu dykes (modified after Duan *et al.* 2019). (c) Simplified geologica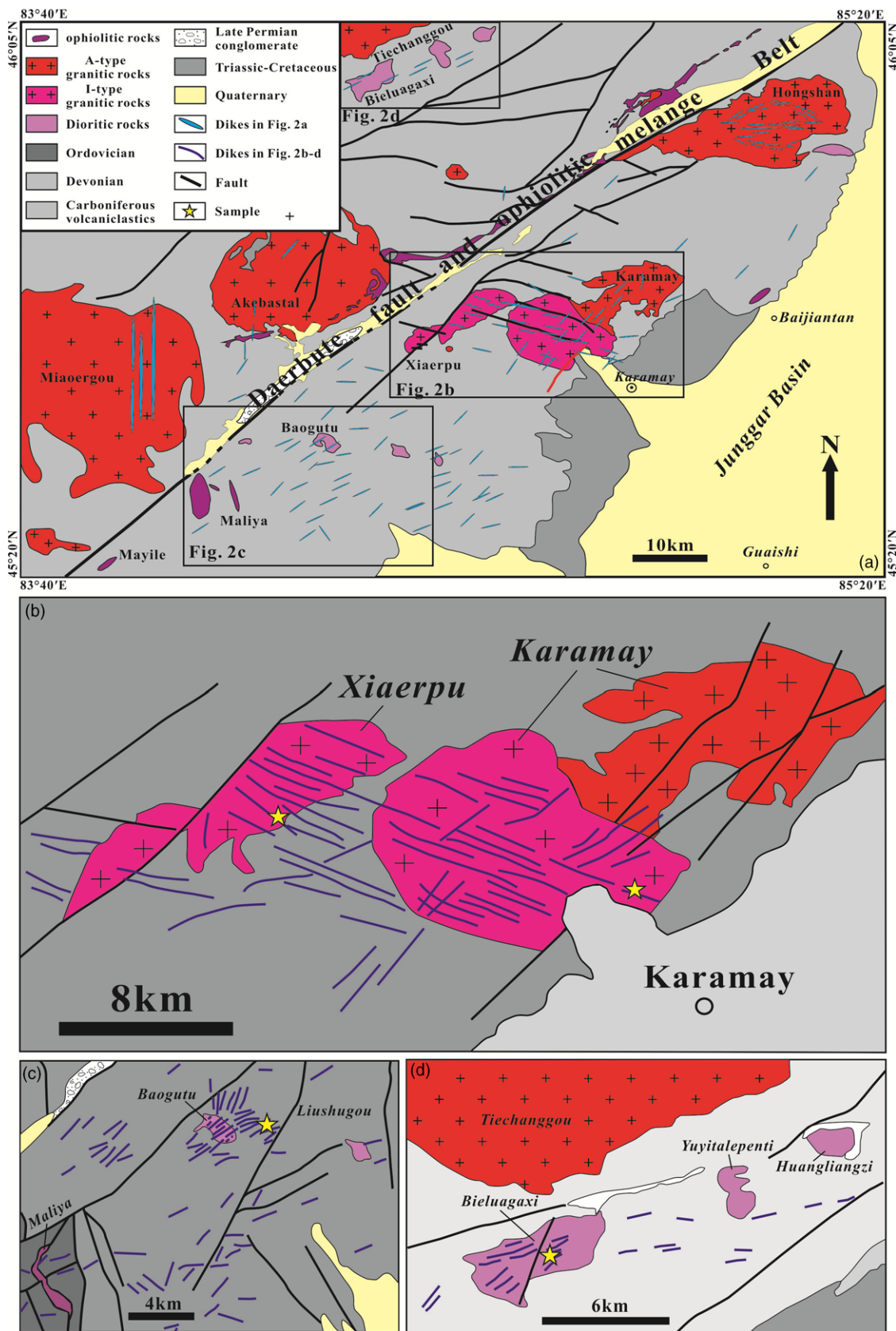l map of the Liushugou dykes (modified after Yin *et al.* 2010). (d) Simplified geological map of the Bieluagaxi dykes (modified after Yin *et al.* 2015a).

environment (Qian & Hermann, 2010). Three major alternative models have been proposed to account for the geochemical characteristics of these West Junggar dykes: (a) partial melting of peridotites metasomatized by slab-derived melts/fluids (Yin *et al.* 2010, 2013, 2015a, 2015b; Tang *et al.* 2012a, 2012b); or (b) sediment-derived melts at a ridge subduction environment (Duan *et al.* 2019) or (c) partial melting of remnant oceanic crust formed in early Palaeozoic during post-collisional processes (Xu *et al.* 2013). Thus, detailed petrological, geochemical and geochronological studies of the dykes in this area could help to resolve which model is most appropriate. Intermediate-mafic dykes usually occur in tensional tectonic regimes, and record information on the timing and processes of continental break-up (Strvastava, 2011). They also can be used to reconstruct the paleostress field and provide information on the genesis and tectonic setting (Ma *et al.* 2012).

In this paper, we present zircon U-Pb ages, elemental and Sr-Nd isotopic data for the Carboniferous dykes in West Junggar (the Karamay, Xiaerpu, Bieluagaxi and Liushugou dykes) to explore their petrogenesis and tectonic implications during the Late Palaeozoic. Based on our new data, we propose that Carboniferous dykes in West Junggar are similar to HMAs and were likely formed by partial melting of peridotites metasomatised by remnant oceanic crust-derived melts or sediment-derived melts in a post-collisional setting.

2. Geological background

The CAOB (Fig. 1a) is located between the Siberian Craton to the north and the Tarim and North China Cratons to the south. It extends from the Urals in the west, through Uzbekistan, Tajikistan, Kazakhstan, NW China, Mongolia and NE China to the Okhotsk Sea in the Eastern Russia (Sengör *et al.* 1993; Jahn *et al.* 2000; Windley, *et al.* 2007). The CAOB is generally thought to be related to the closure of the Palaeo-Asian Ocean because it is a composite terrane made up of diverse fragments including ancient micro-continents, arc terranes, oceanic volcanic islands, volcanic plateaus, oceanic crust and passive continental margin sequences (Coleman, 1989; Buckman & Aitchison, 2004; Windley *et al.* 2007; Choulet *et al.* 2012).

West Junggar is located in the middle of the Kazakhstan orocline (Tang *et al.* 2010; Ma *et al.* 2012) and is surrounded by the Altai orogen to the north, the Tianshan orogen to the south, the Kazakhstan plate to the west, and the Junggar basin to the east (Fig. 1a). Numerous Cambrian to Carboniferous ophiolitic mélanges have been reported from West Junggar (Feng *et al.* 1989; He *et al.* 2007; Yang *et al.* 2012a, 2012b; Zhu *et al.* 2015). Ordovician-Quaternary sedimentary strata are widely distributed in this region, with Devonian-Carboniferous volcano-sedimentary rocks being particularly abundant (BGMRX, 1993). West Junggar can be divided into northern and southern parts by the Xiemisitai Fault (Xu *et al.* 2013; Yin *et al.* 2015a), and some have further divided the southern part of West Junggar into central and southern domains, which recorded different subduction-accretion history (Xu *et al.* 2013; Chen *et al.* 2015). Relatively continuous Carboniferous strata covered by the Permian molasse and continental volcanic rocks with an angular unconformity are dominant in central and southern West Junggar (Zong *et al.* 2016).

Abundant widespread Palaeozoic magmatism and evidence for a prolonged orogenic event are notable characteristics of the West Junggar terrane. Three magmatic pulses have been recognised (Han *et al.* 2006; Chen *et al.* 2010; Gao *et al.* 2014). The oldest Late Devonian – Early Silurian pulse comprises calc-alkaline plutons

and volcanic rocks (Chen *et al.* 2010, 2015; Choulet *et al.* 2012). The middle pulse is composed of Early Carboniferous granitoids, which are characterised by I-type plutons and adakitic rocks and Nb-enriched basalts. The youngest pulse, mostly formed between 310 Ma and 290 Ma, is dominated by A-type granites and sanukitoids, including monzogranite, alkali granite and charnock-ite (Han *et al.* 2006; Geng *et al.* 2009; Chen *et al.* 2010; Tang *et al.* 2012b).

Extensive Late Carboniferous – Early Permian mafic to intermediate dyke swarms are also found in central West Junggar (e.g., Baogutu, Hatu, Akbastal, Xiaerpu, Karamay, Hongshan, Tiechanggou areas) (Yin *et al.* 2010, 2013 2015a, 2015b; Ma *et al.* 2012; Tang *et al.* 2012a; He *et al.* 2015; Li *et al.* 2015; Zhan et al, 2015; Duan *et al.* 2019) (Fig. 2a).

3. Petrological characteristics

The Karamay mafic-intermediate dykes intrude the Late Carboniferous Karamay granitoid and Carboniferous volcano-sedimentary strata (Fig. 2a). Dyke thicknesses range from 0.2 m to 20 m, and are mostly between 1.5 m and 3 m. Although some dykes are a few kilometres in length, most are less than 1 km (Fig. 3a) and mainly trend WNW-ESE (280°-310°) with several dykes trending NE-SW (30°-60°) (Fig. 2b). The NE-SW trending dykes are mainly diorites with minor diabase, whereas the WNW-ESE trending dykes are represented by dioritic porphyry. The NE-SW trending dykes cut across the WNW-ESE trending dykes. No chilled margins against the granitic rocks were observed, but in some places, baked margins can be observed (Fig. 3b). The dykes are generally undeformed and are slightly weathered and chloritized. Compositionally, the diabase exhibits a fine-grained ophitic texture (Fig. 4a) and consists of plagioclase (55–60%[1]), clinopyr-oxene (25–30%), with minor biotite (0–5%), hornblende (0–5%) and magnetite (<5%). The diorite has a massive and fine to medium-grained granular texture and consists of plagioclase (50–55%), hornblende (15–20%), biotite (5–15%) with minor quartz (0–10%), pyroxene (0–5%) and accessory minerals including zircon, magnetite and apatite (Fig. 4b). The dioritic porphyry contains phenocrysts of plagioclase and/or hornblende (15–35%). The matrix (65–35%) is microcrystalline and is composed of plagioclase, hornblende and biotite with minor quartz, pyroxene and Ti-Fe oxides with an aphanitic texture.

Xiaerpu intermediate to mafic dykes are widely distributed in the Xiaerpu granite and adjacent Carboniferous volcanic strata (Figs. 2b and 3c). The Xiaerpu dykes mainly strike 290°–310° (WNW trending) and dip at >80°. They are mostly 0.2 m to 3 m wide with some >5 m. About 5 mm chilled and baked margins against the host granitic rock are well preserved on both sides of some dykes (Fig. 3d). The rock types are dominated by dioritic porphyry and diorite with minor diabase. The dioritic porphyry (Fig. 4c) comprises phenocrysts plagioclase (10–25%) and hornblende (10–35%) set in a fine-grained (<0.02 mm) ground-mass (65–75%). Cleavages and microfractures are limited to the euhedral plagioclase xenocryst interiors without passing through its overgrown rim (Fig. 4d). It is inferred that the xenocrysts and their overgrown rim were formed in original and host magmas respectively and formed by a two-stage process. The diorite has a similar mineralogy to the dioritic porphyry, but has a uniform fine-grained granular texture with plagioclase (55%-60%), hornblende

---

[1]All mineralogical percentages in the paper are in vol.%.
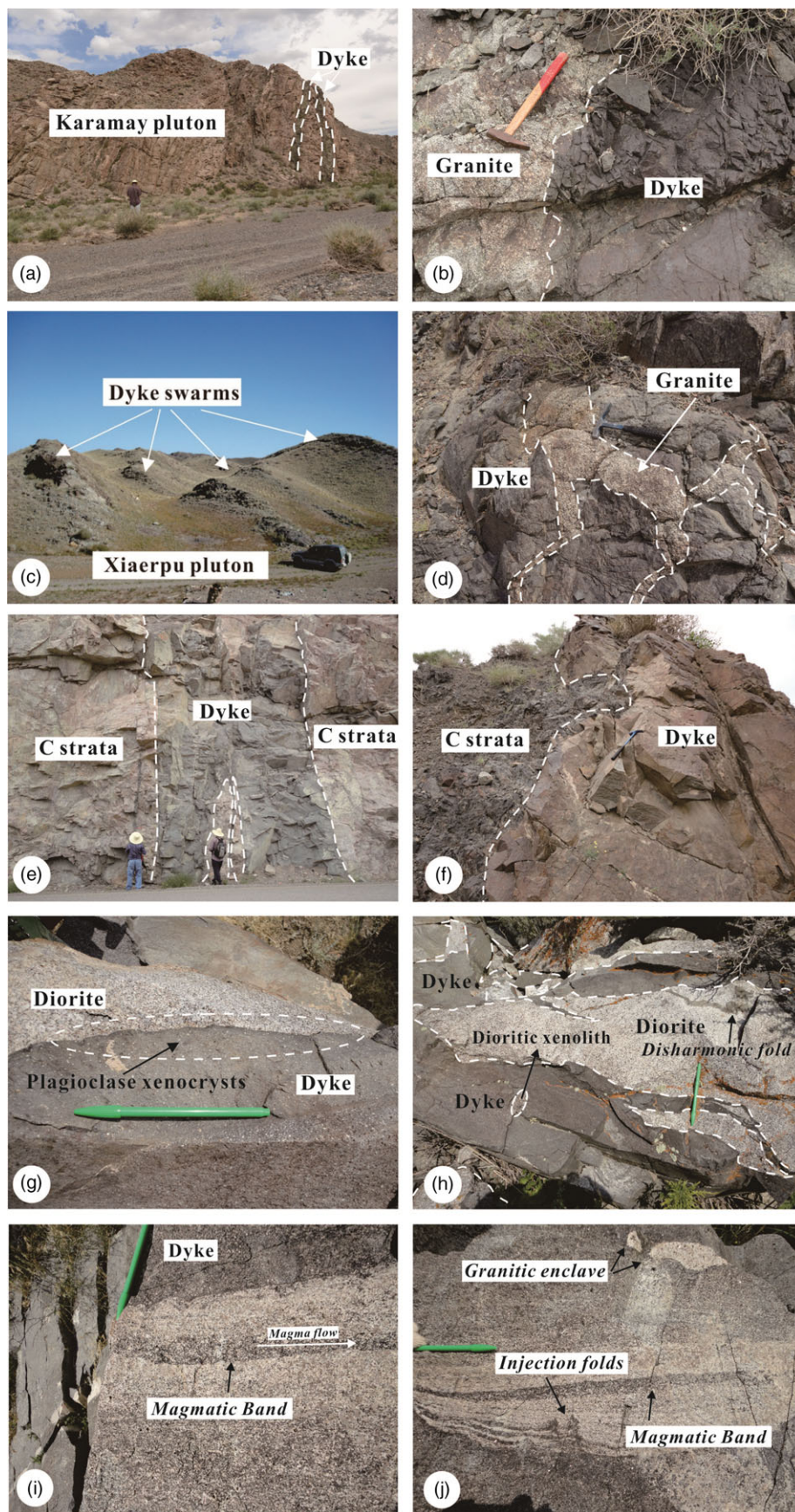
Figure 3. (Colour online) Outcrop photos of dykes and their host plutons. (a) Dykes intruded into the Karamay pluton. (b) Baked and chilled margins on the contact boundary between the dyke and the host rocks. (c) Dyke swarms intruded into Xiaerpu pluton. (d) Granitic as enclaves surrounded by the dyke. (e) Dykes intruded Lower Carboniferous strata (abbreviated and marked as C strata in the photo) in Liushugou area. (f) Intrusive contact between a NE-SW dyke and the Lower Carboniferous strata. (g) Bieluagaxi diorite intruded by the dyke with plagioclase xenocrysts on the edge of the dyke. (h) The dykes and the diorite interpenetrated with each other, and dioritic enclave and disharmonic fold. (i) The straight magmatic bands as orientation of aligned hornblende showing magma flow in the host Bieluagaxi granitic rocks. (j) The straight and curved magmatic bands with injection folds and granitic enclaves in the host Bieluagaxi granitic rocks.
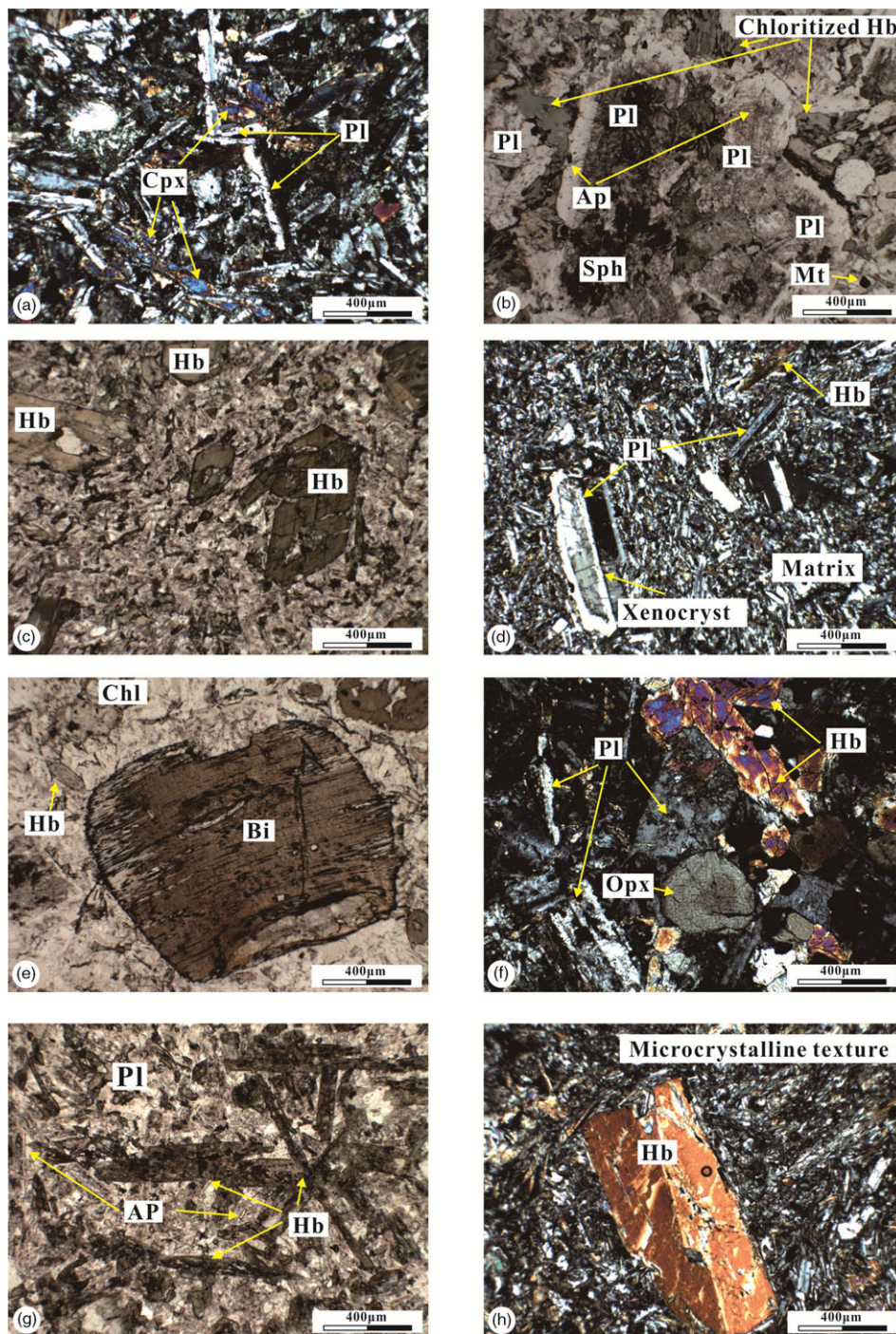
Figure 4. (Colour online) Microscopic photos of the dykes in the West Junggar. (a) Typical diabasic texture that xenomorphic clinopyroxenes filling in the spaces between the semi-euhedral acerose plagioclases, in Karamay dolerite dyke under the cross-polarised light. (b) Plagioclase, chloritized Hb with Ap, Sph and Mt in the Karamay dioritic dyke under the single-polarised light. (c) Porphyritic texture that phenocryst mainly consists of idiomorphic Hb crystals of the Xiaerpu dioritic porphyrite in the single-polarised light. (d) Mineral assemblages of the Xiaerpu dioritic porphyritic dyke in the cross-polarized light. Phenocryst consists of Pl and Hb, and the matrix shows microcrystalline texture with numerous acicular plagioclases and mafic minerals. (e) Hypidiomorphic sheet biotite as the phenocryst in dioritic porphyrite in Liushugou dioritic porphyrite in the single-polarised light. (f) Fine-grained granular texture with mineral assemblages of Pl, Hb and Opx in the Liushugou dioritic dyke under the cross-polarised light. (g) Long columnar Hb and plate-shaped Pl in the Bieluagaxi dioritic dyke under the single-polarised light. The euhedral amphiboles and acicular apatites embedded in the plagioclase indicate that the magma of dioritic dyke was initially quenched into the unconsolidated host granitic magma and then slowly cooled with it. (h) Porphyritic texture with twining Hb as phenocryst in the Bieluagaxi dioritic porphyritic dyke in the cross-polarised light. Pl = plagioclase, Opx = orthopyroxene, Cpx = Clinopyroxene, Hb = hornblende, Bi = biotite, Ap = apatite, Chl = chlorite, Sph = sphene, Mt = magnetite.

(25–30%), alkali feldspar (5–10%), biotite (0–10%) and quartz (0–5%). The diabase consists of diopside (35–40%), sericitized plagioclase (50–55%), Ti-Fe oxides (5–10%) and minor hornblende (5%) and biotite (<5%). The diabase has ophitic texture with anhedral mafic minerals and Ti-Fe oxides filling in the spaces between the plagioclase laths.

A large number of dykes are found in the Liushugou area, but their distribution is dispersed compared with those of the Karamay and Xiaerpu areas. The Liushugou dykes are generally undeformed and range in width from 0.5 m to 4 m and in length from 0.1 km to 1.5 km. They mainly trend in a NE direction (Fig. 3g), with minor dykes trending to the WNW (Fig. 2d). The NE-trending dykes are diorites, and the NW trending ones are represented by dioritic porphyries. The dykes intrude Carboniferous and Ordovician sediments, the Maliya ophiolitic mélange and the Baogutu dioritic intrusion. Chilled and baked margins are not obvious between the country rocks and the dykes (Fig. 3h). Petrographically, the dykes are fine-grained diorite and dioritic porphyry and have undergone slight chloritization and sericitization. The diorite has a massive and fine to medium-grained granular texture (Fig. 4f) and consists of plagioclase (45–55%), hornblende (25–35%), quartz (<5%), orthopyroxene (0–5%) and accessory minerals such as magnetite (<3%) and apatite (<3%). The dioritic porphyry comprises 15–25% plagioclase and/or hornblende are phenocrysts, and the aphanitic matrix (75–85%) consists of plagioclase (55–65%), hornblende (30–45%) with minor quartz (<5%), pyroxene (<5%) and opaque minerals (<5%).

The Bieluagaxi dykes (Fig. 2e) are located about 1.5 km south of the Tiechanggou granite and trend ENE (60°–80°), which is parallel to the NE-trending regional faults. The dykes intrude the Devonian Kulumudi formation and small Bieluagaxi dioritic pluton and range in width from 0.2 m to 3 m, and in length from 0.1 km to 2 km. Both baked and chilled margins are found between the host pluton and the dykes. Several granular plagioclase xenocrysts were also observed on the margin of dykes against the host pluton (Fig. 3i), indicating that some magma mixing occurred between the parental magma of the Bieluagaxi pluton and the magma of the dykes. In some places, dykes have been intruded by the pluton (Fig. 3j), implying that they are coeval. The dyke swarms mostly include diorite, dioritic porphyry, with a few diabase dykes also being found. The diorite has a massive and fine-grained granular texture (Fig. 4g) with plagioclase (50–60%), hornblende (30–35%), biotite (0–5%), quartz (0–5%) and accessory minerals *e.g.,* opaque minerals (<5%), apatite (<3%) and epidote (<3%). Dioritic porphyry displays massive and porphyritic textures (Fig. 4h). The phenocrysts (20–40%) consist of plagioclase (15–25%) and hornblende (5–15%), set in a microcrystalline matrix (60–80%) with needle-like plagioclase (45–55%), hornblende (15–25%) and minor alkal feldspar (5%). The diabases exhibit typical ophitic and massive textures and comprise diopside (35–45%), sericitised plagioclase (50–55%) and Ti-Fe oxides (5–10%) with minor hornblende (0–5%) and biotite (0–5%).

The GPS and detailed observations of dykes in central West Junggar are listed in Table S1 and Fig. 4, respectively.

4. Results

4.a Zircon U-Pb geochronology

Four samples from the dykes in West Junggar were selected for U-Pb zircon dating, and the results are listed in Table 1. The descriptions of the analytical methods used are given in Appendix 1. The zircon CL images and the concordia diagrams are presented in Figs. 5 and 6, respectively. All confidence intervals are reported at 95%.

Zircons in the Karamay dyke (sample KM1510N; GPS: E84°44′04″, N45°39′39″) are euhedral and prismatic with concentric oscillatory zoning and are 90–180 μm in length (Fig. 5a). The zircons have a high concentration of Th and U with Th/U ratios of 0.38–0.52. Nineteen spots form a cluster on a concordia diagram with $^{206}Pb/^{238}U$ ages ranging from 305.4 Ma to 316.4 Ma (Fig. 6a, inset) and a weighted mean $^{206}Pb/^{238}U$ age of 311.3±2.1 Ma with an MSWD of 0.74.

Zircons from Xiaerpu dyke (sample XP1505N; GPS: E84°36′18″, N45°42′35″) are transparent to pale yellow, euhedral columnar crystals. All show typical oscillatory zoning in the CL images, are 100–200 μm in length and width/length ratios ranging from 1:2 to 1:3 (Fig. 5b). Zircon grains have Th contents ranging from 204 to 522 ppm and U contents ranging from 242 to 930 ppm with relatively high Th/U ratios of 0.35–0.85. Fourteen spots yield a weighted mean $^{206}Pb/^{238}U$ age of 309.7±2.4 Ma (Fig. 6b, inset) with MSWD of 1.08.

Zircons from the Bieluagaxi dyke (sample BLG1505N; GPS: E84°24′19″, N46°02′09″) are prismatic and euhedral crystals with rhythmic oscillatory zoning and are 85–180 μm in length (Fig. 5c). The zircons have high U and Th contents with relatively high Th/U ratios (0.55–0.75). Thirteen spots yield a weighted mean $^{206}Pb/^{238}U$ age of 324.3±3.6 Ma (Fig. 5c) with MSWD of 0.94.

Zircons from Liushugou dyke (sample LSG1501N; GPS: E84°17′40″, N45°30′59″) show internal oscillatory zonation. They are 100–200 μm in length and are mostly subhedral-euhedral prismatic crystals (Fig. 5h). They have high Th/U contents of 0.55–1.18, indicating a magmatic origin. Seventeen spots of sample LSG1501N yield a weighted mean $^{206}Pb/^{238}U$ age of 313.9±3.2 Ma with an MSWD of 0.31 (Fig. 6h).

4.b Whole-rock geochemistry

Analytical methods are described in Appendix 1 and the whole-rock elemental data for the dykes in the West Junggar area are shown in Table 2 and S4. A few samples have relatively high LOI values of 3.00–5.37 wt.%, however, most samples have LOI values of 1.88–2.99 wt.%, (Table 2), supporting a low degree of alteration or low-grade metamorphism. The major oxides and trace elements do not display any obvious correlations with LOI values (Table S2 and Fig. S1), further suggesting that their abundances are unlikely to have been modified by the low-grade metamorphism or alteration.

The dykes in West Junggar have variable low – intermediate SiO_2 (52.3 – 60.9 wt.%), moderate – high Al_2O_3, and along with relatively low TiO_2 and FeO^T (Table 2). They have low Nb/Y ratios of 0.13–0.31 (except sample BLG1502 with Nb/Y = 0.85) and plot in the fields of andesite and andesite/basalt on the Nb/Y vs. Zr/TiO_2 diagrams (Fig. 7a). The dykes have moderate total alkali content (ALK = Na_2O+K_2O) ranging from 3.69 and 5.72 wt.% with Na_2O/K_2O ratios of 2.14–7.23 and are classified as gabbroic diorite (Liushugou and Bieluagaxi dykes) and diorite (Karamay and Xiaerpu dykes) in the ALK vs. SiO_2 diagram (not shown). Most of the dykes show medium-K calc-alkaline and minor with high-K calc-alkaline and arc tholeiite characteristics (Fig. 7b). They possess variable MgO contents between 2.6 wt.% and 8.4 wt.% with $Mg\#$ of 51–69 ($Mg\# = 100*Mg^{2+}/(Mg^{2+}+Fe^{2+})$) and low ratios of $(La/Yb)_N$ (3.6 – 14.0), consistent with many of the features of HMAs (McCarron & Smellie, 1998; Kelemen *et al.* 2003; Kamei *et al.* 2004).

Table 1. Whole rock major (wt. %) and trace (ppm) element of Late Carboniferous dykes in West Junggar

No.	1	2	3	4	5	6	7	8	9	10	11	12	13
Region	Karamay		Xiaerpu				Bieluagaxi			Liushugou			
Sample No.	KM1503	KM1510	XP1501	XP1505	XP1507	XP1510	BLG1502	BLG1505	BLG1507	LSG1501	LSG1502	LSG1504	LSG1505
Lithology	Dioritic Porphyrite	Dioritic Porphyrite	Dioritic Porphyrite	Dioritic Porphyrite	Dioritic Porphyrite	Dioritic Porphyrite	Dolerite	Diorite	Dioritic Porphyrite	Diorite	Diorite	Dioritic Porphyrite	Dioritic Porphyrite
Major oxides													
SiO_2	60.94	59.35	59.27	57.53	58.62	57.16	52.97	52.30	54.59	53.93	55.70	55.18	55.20
TiO_2	0.56	0.76	0.78	0.70	0.77	0.75	1.38	1.09	0.61	0.92	0.90	0.80	0.82
Al_2O_3	17.19	16.36	16.41	17.09	17.42	16.94	15.29	15.78	14.81	16.54	16.18	15.94	16.43
Fe_2O_3	1.36	2.18	2.03	1.49	1.28	1.37	3.30	0.95	0.97	2.73	1.69	1.49	1.42
FeO	3.07	3.67	3.83	4.90	4.63	4.47	4.75	6.27	5.87	4.43	4.57	4.37	5.27
MnO	0.07	0.10	0.09	0.11	0.07	0.09	0.14	0.12	0.15	0.13	0.10	0.09	0.11
MgO	2.56	4.28	4.08	4.54	3.29	4.11	5.63	7.91	8.41	5.20	6.12	5.62	5.28
CaO	5.29	5.95	5.60	6.46	6.35	6.56	6.02	6.73	7.10	8.06	5.02	5.60	6.26
Na_2O	3.72	3.21	3.50	3.19	3.72	3.67	3.98	3.43	2.67	3.42	4.45	4.16	3.91
K_2O	1.55	1.35	1.57	1.19	0.74	1.11	1.74	1.46	1.02	1.60	0.62	0.86	1.20
P_2O_5	0.11	0.15	0.15	0.14	0.19	0.15	0.46	0.22	0.12	0.17	0.18	0.17	0.16
H_2O^+	2.13	2.08	1.92	2.14	1.92	2.36	2.67	2.70	2.50	2.37	2.86	3.05	2.52
CO_2	1.13	0.18	0.47	0.27	0.82	0.92	0.98	0.72	0.57	0.04	0.98	2.06	1.03
Total	99.69	99.61	99.71	99.75	99.82	99.67	99.31	99.68	99.38	99.54	99.36	99.39	99.60
FeO^T	4.30	5.63	5.66	6.24	5.79	5.70	7.72	7.13	6.74	6.88	6.09	5.71	6.55
ALK	5.27	4.56	5.07	4.37	4.46	4.78	5.72	4.89	3.69	5.03	5.07	5.03	5.11
A/CNK	0.99	0.93	0.93	0.93	0.94	0.88	0.79	0.81	0.80	0.75	0.94	0.89	0.86
Mg#	59.8	67.5	65.5	62.3	55.8	62.1	67.9	69.2	71.9	67.7	70.5	69.6	64.1
FeOT/MgO	1.68	1.32	1.39	1.38	1.76	1.39	1.37	0.90	0.80	1.32	0.99	1.02	1.24
Trace elements													
Li	32.7	37.9	16.1	22.2	17.2	16.0	25.7	27.1	34.8	10.0	34.5	19.9	22.6
Be	0.82	0.74	0.88	0.63	0.69	0.62	1.44	1.10	0.90	0.74	0.58	0.75	0.62
Sc	11.5	15.6	13.5	16.5	14.4	17.0	18.1	18.2	25.4	21.6	16.4	14.9	17.6
V	99.0	148	135	161	146	159	166	115	153	195	157	133	163
Cr	34.7	146	127	93.4	26.0	69.2	133	312	402	121	276	231	162
Co	14.8	21.9	22.1	23.7	19.3	21.4	27.6	27.0	28.6	25.4	27.2	26.5	27.5
Ni	29.1	72.6	73.9	71.4	34.9	50.6	94.3	135	113	43.6	159	144	100

(Continued)

Table 1. (*Continued*)

|													
Cu	47.2	64.3	56.2	11.8	19.3	33.3	59.3	7.65	8.47	52.7	68.5	61.1	13.9
Zn	51.9	70.7	63.0	52.1	36.0	53.2	126	40.0	62.5	50.3	61.9	65.5	67.5
Ga	18.9	20.3	18.7	19.6	20.5	19.0	21.1	16.2	15.9	20.5	21.3	19.1	20.4
Rb	34.0	28.1	37.1	39.3	18.0	32.0	32.2	31.5	26.3	40.0	13.6	18.2	19.5
Sr	606	641	564	643	671	697	618	463	294	681	748	647	715
Y	9.59	13.2	12.6	9.81	11.3	10.6	18.2	20.4	15.4	16.8	9.03	11.0	11.8
Zr	93.0	104.6	117.3	58.2	81.3	67.6	179.9	134.4	86.4	80.7	55.2	72.3	71.4
Nb	2.19	2.59	3.12	1.44	2.48	1.66	15.5	6.39	3.77	2.50	1.23	1.11	1.53
Sn	0.64	0.73	0.69	2.47	1.08	0.54	1.71	0.59	1.05	0.87	0.59	0.59	0.57
Cs	1.07	0.99	0.84	1.71	0.77	0.88	0.80	1.02	0.93	0.75	0.68	0.46	0.20
Ba	642	431	477	382	421	376	503	358	395	438	1163	465	446
La	10.6	9.87	11.1	6.40	7.34	5.89	33.7	11.3	9.40	8.86	5.56	5.49	6.60
Ce	22.0	22.4	24.5	13.9	17.1	14.1	68.3	25.7	20.9	20.6	13.7	14.0	15.6
Pr	2.59	2.88	3.14	1.90	2.28	1.92	8.00	3.41	2.55	2.70	1.96	2.04	2.18
Nd	10.8	12.8	13.5	8.62	10.4	9.12	31.8	14.6	10.6	12.0	9.53	9.39	10.0
Sm	2.21	2.92	3.06	2.01	2.47	2.24	5.82	3.68	2.49	3.12	2.37	2.36	2.38
Eu	0.62	0.81	0.83	0.65	0.79	0.74	1.56	1.19	0.81	0.98	0.69	0.81	0.79
Gd	1.90	2.50	2.57	1.82	2.51	2.18	4.30	3.42	2.42	3.02	2.00	2.23	2.24
Tb	0.32	0.41	0.40	0.28	0.35	0.34	0.64	0.63	0.46	0.52	0.32	0.35	0.36
Dy	1.81	2.53	2.42	1.80	2.13	2.03	3.59	3.73	2.71	3.02	1.78	2.02	2.21
Ho	0.34	0.49	0.45	0.34	0.41	0.39	0.65	0.72	0.58	0.61	0.36	0.42	0.40
Er	1.00	1.46	1.30	1.00	1.18	1.10	1.81	2.00	1.63	1.69	0.91	1.14	1.17
Tm	0.14	0.20	0.17	0.13	0.16	0.15	0.27	0.29	0.27	0.27	0.15	0.16	0.18
Yb	0.86	1.32	1.17	0.94	1.09	0.98	1.72	2.05	1.69	1.67	0.87	1.10	1.12
Lu	0.14	0.19	0.16	0.13	0.15	0.14	0.26	0.31	0.26	0.27	0.14	0.15	0.18
Hf	2.62	2.96	3.11	1.66	2.22	2.02	4.49	3.28	2.36	2.29	1.59	1.95	1.91
Ta	0.20	0.18	0.21	0.097	0.17	0.11	0.79	0.46	0.28	0.16	0.085	0.068	0.11
Tl	0.25	0.17	0.21	0.21	0.12	0.17	0.17	0.14	0.14	0.22	0.090	0.11	0.11
Pb	7.66	5.94	3.90	2.23	3.26	2.86	7.25	2.59	3.20	2.82	2.08	2.96	2.46
Th	3.31	2.40	2.73	1.15	1.14	0.94	7.37	2.16	2.67	1.83	0.63	0.77	0.97
U	1.22	0.90	0.98	0.54	0.45	0.41	1.64	0.67	0.56	0.40	0.23	0.34	0.38
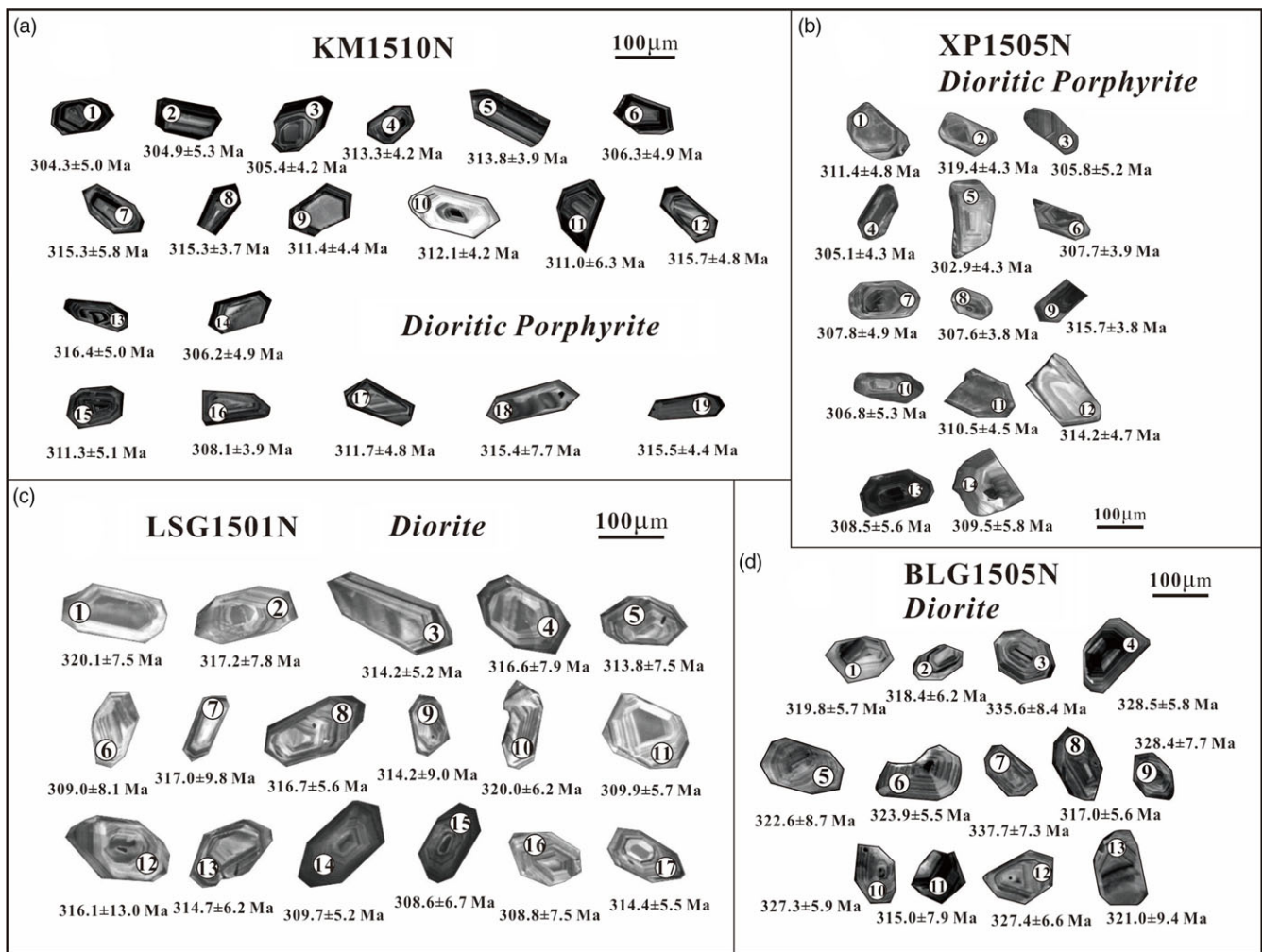
Figure 5. Cathodoluminescence (CL) images of zircons from Carboniferous dykes in West Junggar.

Based on the distribution according to their orientation, petrology and geochronology of dykes in West Junggar, they can be divided into three groups (Table S1): the Early stage is represented by ENE-trending Bieluagaxi dykes, which were generated at 324 Ma and include diorite, dioritic porphyrite, with minor diabase; the Late 1 stage contains WNW-trending dykes formed between 314 Ma and 310 Ma, including dioritic porphyrites in Karamay, Xiaerpu and Liushugou areas; the last stage is referred as Late 2 stage marked by relatively younger NE-trending diorite with minor diabase dykes (<310 Ma) in Karamay and Liushugou areas.

In view of the similar geochemical characteristics of the Late 1 and 2 stage dykes (Figs. 6–8, Table 2 and S4), we divide dykes in West Junggar into two groups. Karamay, Xiaerpu and Liushugou dykes (Group 1: Late 1 and 2 stage) and Bieluagaxi dykes (Group 2: Early stage).

Group 1 samples have relatively low – moderate rare earth element (REEs) concentrations (ΣREE 40 – 65 ppm). They display coherent REE patterns that are enriched in the LREEs [(La/Yb) $_N$ = 3.6 – 8.9] with depleted HREE patterns [(Gd/Yb) $_N$ = .50 – 1.90] and slightly negative to positive Eu anomalies (0.9 – 1.1) (Table 2; Fig. 10a, c and g). They have variable Cr (26 – 276 ppm) and Ni (29 – 159 ppm), high Sr (564 – 748 ppm), Sr/Y ratios of 40.5 – 82.9 (Yin *et al.* 2010, 2013; Ma *et al.* 2012; Tang *et al.* 2012a) and Ba (376 – 1163 ppm) with depletion in Yb (0.86 – 1.67 ppm) and Y (9.03 – 16.8 ppm) (Table 2).

Group 2 rocks are also enriched in LREE relative to HREE with (La/Yb) $_N$ ratios of 3.94–14.03 and (Gd/Yb) $_N$ ratios of 1.19–2.06 (Table 2; Fig. 10e) along with weak negative to weak positive Eu anomalies (Group 1: Eu*/Eu = 0.88–1.07; Group 2 of 0.91–1.01). Compared with Group 1 samples, they have similar Cr and Ni contents but lower Sr (294–618 ppm), Ba (358–503 ppm) and Sr/Y ratios of 19.1–33.9 (Fig. 8b). On primitive mantle-normalised multi-element diagrams (Fig. 10), Group 1 as well as being enriched in Light Rare Earth Element (LREE) and Large Ion Lithophile Element (LILE) are depleted in High Field Strength Element (HFSE, e.g., Nb and Ta) (Fig. 10b, d and h). Group 2 samples have a similar pattern to Group 1 rocks but with relatively lower Nb and Ta, and higher Sr and Ba (Fig. 10f).

In summary, all studied dykes resemble HMAs and are characterised by intermediate SiO$_2$, high MgO, high Cr and Ni contents, marked Nb and Ta depletions, high Sr, Ba and highly fractionated REE (Martin *et al.* 2005; Yin *et al.* 2010).

4.c Sr-Nd isotopes

Analytical methods for whole-rock Sr-Nd analyses are given in Appendix 1. Eight representative dyke samples were analysed for Sr and Nd isotopes and these results are listed in Table 3. All measured ^{87}Sr/^{86}Sr ratios and εNd values have been corrected to the corresponding ages of dykes (Table 3; Fig. 11a). The (^{87}Sr/^{86}Sr) $_i$
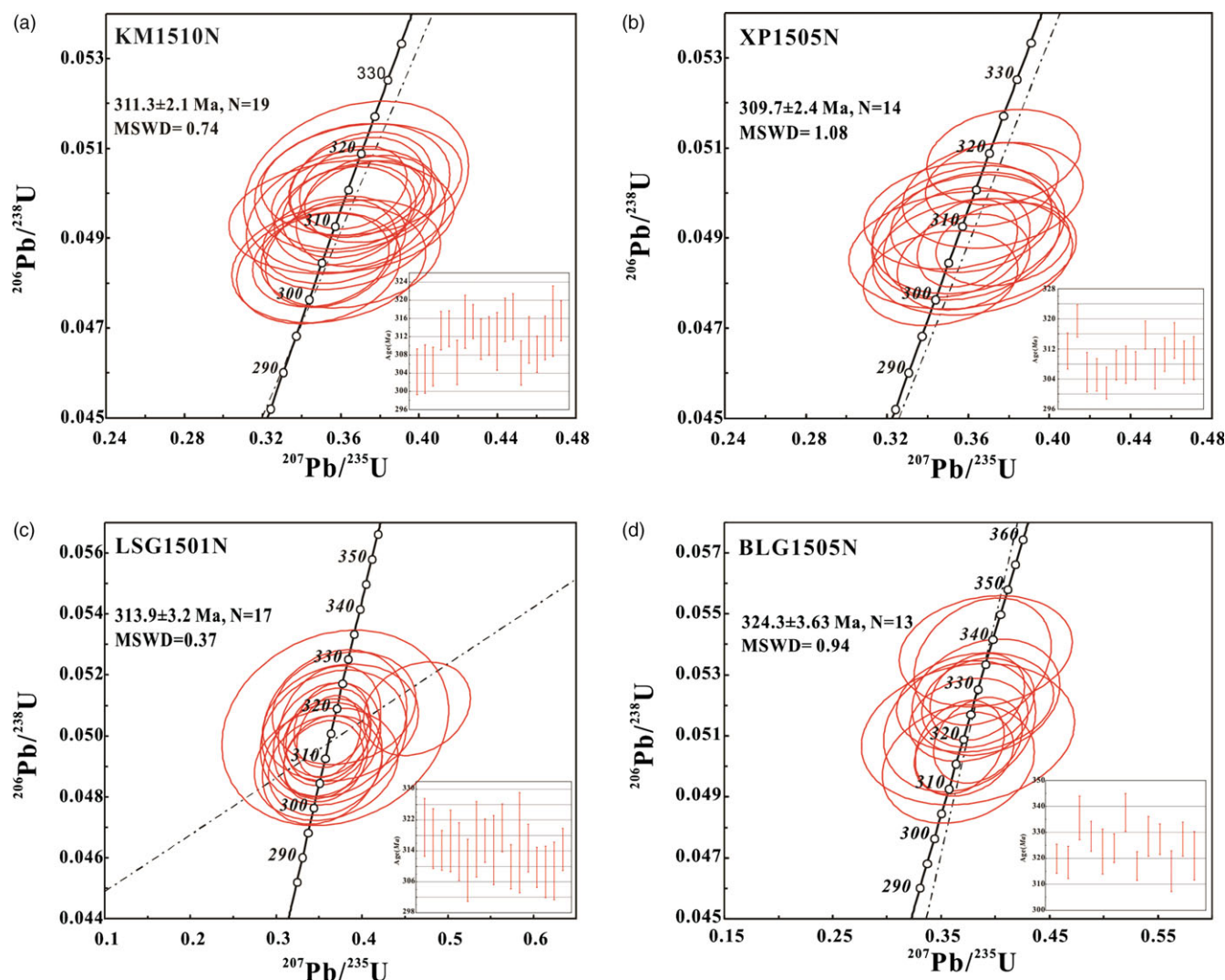
Figure 6. (Colour online) U-Pb Concordia diagrams showing zircon ages obtained by LA-ICP-MS for dykes in West Junggar.

ratios of the Karamay dykes range from 0.7035 to 0.7039, with an εNd(*t*) value of + 7.8 and the Nd model age (T_{DM}) of 0.52 Ga. The Xiaerpu dykes exhibit εNd(*t*) values of +4.5 − +7.0, ($^{87}Sr/^{86}Sr$)$_i$ ratios of 0.7037−0.7039 and T_{DM} of 0.58 − 0.83 Ga. The Bieluagaxi dykes have ($^{87}Sr/^{86}Sr$)$_i$ ratios of 0.7041 to 0.7044 and positive εNd(*t*) values ranging from +4.4 to +5.7 with T_{DM} of 0.62−0.69 Ga. The Liushugou dykes have εNd(*t*) values between +5.2 and +7.4, ($^{87}Sr/^{86}Sr$)$_i$ ratios ranging from 0.7038 to 0.7044 and T_{DM} from 0.53 to 0.77 Ga. Thus, all studied dykes in West Junggar have positive εNd(*t*) values (+4.4 to +7.8), low ($^{87}Sr/^{86}Sr$)$_i$ ratios (0.7035 − 0.7044) and young Nd model ages (T_{DM} = 0.52 − 0.83 Ga).

5. Discussion

5.a Age correlation between dykes and host rocks

The zircons from the dykes in West Junggar have high Th/U ratios (Table 1) with oscillatory zoning shown by the CL images (Fig. 5), suggesting magmatic origins. However, most of the zircons in the dykes show typical alternating light and dark oscillatory zoning to those in the felsic magmatic rocks. The ages of zircons from the

dykes are similar to the host granitic rocks, and so it is possible that the dated zircons in dykes were captured by the Carboniferous granitic host rocks. This conclusion is supported by the geological intercalated relationship between the dykes and the host granitic rocks. Both the dykes and the host granitic rocks underwent plastic interactions, indicating that the host rocks were still semi-crystalline, and even hot, when the dykes were emplaced (Ma *et al.* 2012). Therefore, based on the weighted average $^{206}Pb/^{238}U$ age of zircons (Karamay dykes, 311 Ma; Xiaerpu dykes, 310 Ma; Bieluagaxi dykes, 324 Ma; Liushugou dykes, 314 Ma), and the field relationship between the dykes and the host granitic rocks, the dykes were formed almost simultaneously or slightly later than the host granitic rocks in the Late Carboniferous.

All studied dykes intrude into their corresponding host plutons except for the Liushugou dykes, which intrude into Devonian to Carboniferous strata (Fig. 2d). The Late Carboniferous – Early Permian host rocks (e.g., Karamay, Xiaerpu, Hongshan and Bieluagaxi granitoid complexes) in West Junggar are well-dated (Table S3) and consist of syenogranite + alkali-feldspar granite ± monzogranite ± granodiorite ± diorite. These granitoids have emplacement ages between 276 Ma and 319 Ma (Table S3). Based on reported data (Chen & Jahn, 2004; Han *et al.* 2006; Geng et al,

Table 2. Zircon U-Pb LA-ICP-MS geochronological data of Late Carboniferous dykes in West Junggar

Number	Pb Total ppm	Th 232 ppm	U 238 ppm	Th/U	Isotopic Ratios						Age (Ma)					
					$^{207}Pb/^{206}Pb$ Ratio	$^{207}Pb/^{206}Pb$ 1sigma	$^{207}Pb/^{235}U$ Ratio	$^{207}Pb/^{235}U$ 1sigma	$^{206}Pb/^{238}U$ Ratio	$^{206}Pb/^{238}U$ 1sigma	$^{207}Pb/^{206}Pb$ Age (Ma)	$^{207}Pb/^{206}Pb$ 1sigma	$^{207}Pb/^{235}U$ Age (Ma)	$^{207}Pb/^{235}U$ 1sigma	$^{206}Pb/^{238}U$ Age (Ma)	$^{206}Pb/^{238}U$ 1sigma
Karamay																
KM1510N-1	34	160	319	0.50	0.05387	0.00431	0.34861	0.02760	0.04834	0.00082	364.9	212.0	303.7	20.8	304.3	5.0
KM1510N-2	21	89	222	0.40	0.05530	0.00517	0.35388	0.03269	0.04843	0.00087	433.4	204.6	307.6	24.5	304.9	5.3
KM1510N-3	46	216	416	0.52	0.05330	0.00366	0.34979	0.02300	0.04852	0.00069	342.7	155.5	304.6	17.3	305.4	4.2
KM1510N-4	46	200	441	0.45	0.05350	0.00399	0.36381	0.02579	0.04980	0.00069	350.1	168.5	315.1	19.2	313.3	4.2
KM1510N-5	43	195	409	0.48	0.05462	0.00318	0.37502	0.02211	0.04987	0.00064	398.2	129.6	323.4	16.3	313.8	3.9
KM1510N-6	46	210	448	0.47	0.05360	0.00355	0.35511	0.02219	0.04867	0.00079	353.8	150.0	308.6	16.6	306.3	4.9
KM1510N-7	46	219	446	0.49	0.05393	0.00504	0.36588	0.03293	0.05012	0.00095	368.6	211.1	316.6	24.5	315.3	5.8
KM1510N-8	77	348	690	0.50	0.05307	0.00258	0.36631	0.01808	0.05013	0.00061	331.5	111.1	316.9	13.4	315.3	3.7
KM1510N-9	51	235	455	0.52	0.05411	0.00347	0.36096	0.02301	0.04950	0.00072	376.0	144.4	312.9	17.2	311.4	4.4
KM1510N-10	59	262	588	0.45	0.05320	0.00327	0.36426	0.02248	0.04961	0.00069	344.5	140.7	315.4	16.7	312.1	4.2
KM1510N-11	26	115	260	0.44	0.05359	0.00485	0.36258	0.03351	0.04942	0.00103	353.8	173.1	314.1	25.0	311.0	6.3
KM1510N-12	52	226	495	0.46	0.05573	0.00384	0.37021	0.02388	0.05019	0.00077	442.6	153.7	319.8	17.7	315.7	4.8
KM1510N-13	30	127	320	0.40	0.05475	0.00500	0.37065	0.03386	0.05030	0.00082	466.7	205.5	320.1	25.1	316.4	5.0
KM1510N-14	41	174	413	0.42	0.05225	0.00629	0.36513	0.03025	0.04865	0.00079	298.2	251.8	316.0	22.5	306.2	4.9
KM1510N-15	25	111	280	0.40	0.05335	0.00533	0.36033	0.03797	0.04947	0.00083	342.7	225.9	312.5	28.3	311.3	5.1
KM1510N-16	64	263	609	0.43	0.05302	0.00370	0.35666	0.02406	0.04896	0.00064	327.8	159.2	309.7	18.0	308.1	3.9
KM1510N-17	51	219	460	0.48	0.05503	0.00337	0.37198	0.02298	0.04955	0.00078	413.0	106.5	321.1	17.0	311.7	4.8
KM1510N-18	41	152	399	0.38	0.05323	0.00536	0.36786	0.03791	0.05014	0.00126	338.9	226.8	318.1	28.1	315.4	7.7
KM1510N-19	51	226	492	0.46	0.05249	0.00307	0.36793	0.02284	0.05016	0.00072	305.6	133.3	318.1	17.0	315.5	4.4
Xiaerpu																
XP1505N-1	39	205	284	0.72	0.05368	0.00468	0.35487	0.03046	0.04950	0.00078	366.7	198.1	308.4	22.8	311.4	4.8
XP1505N-2	63	347	461	0.75	0.05415	0.00357	0.37736	0.02496	0.05080	0.00070	376.0	150.0	325.1	18.4	319.4	4.3
XP1505N-3	43	216	299	0.72	0.05443	0.00524	0.36217	0.03246	0.04859	0.00085	390.8	212.0	313.8	24.2	305.8	5.2
XP1505N-4	54	280	448	0.63	0.05353	0.00325	0.35763	0.02154	0.04847	0.00070	350.1	137.0	310.4	16.1	305.1	4.3
XP1505N-5	58	313	404	0.78	0.05259	0.00387	0.34642	0.02511	0.04811	0.00069	322.3	138.9	302.0	18.9	302.9	4.3
XP1505N-6	83	323	930	0.35	0.05362	0.00253	0.35962	0.01626	0.04889	0.00064	353.8	100.9	311.9	12.1	307.7	3.9
XP1505N-7	56	292	459	0.64	0.05318	0.00394	0.35429	0.02385	0.04891	0.00080	344.5	163.9	307.9	17.9	307.8	4.9
XP1505N-8	77	442	528	0.84	0.05548	0.00322	0.37706	0.02176	0.04887	0.00061	431.5	134.2	324.9	16.0	307.6	3.8

(*Continued*)

Table 2. (*Continued*)

XP1505N-9	89	522	616	0.85	0.05407	0.00327	0.37167	0.02157	0.05019	0.00061	372.3	137.0	320.9	16.0	315.7	3.8
XP1505N-10	33	204	242	0.84	0.05315	0.00543	0.35722	0.03697	0.04874	0.00087	344.5	231.5	310.1	27.7	306.8	5.3
XP1505N-11	45	216	405	0.53	0.05432	0.00413	0.36155	0.02626	0.04935	0.00073	383.4	167.6	313.4	19.6	310.5	4.5
XP1505N-12	55	240	453	0.53	0.05350	0.00422	0.37204	0.02935	0.04995	0.00077	350.1	179.6	321.2	21.7	314.2	4.7
XP1505N-13	40	206	290	0.71	0.05449	0.00494	0.35891	0.03061	0.04902	0.00092	390.8	205.5	311.4	22.9	308.5	5.6
XP1505N-14	43	250	321	0.78	0.05343	0.00470	0.35999	0.03127	0.04919	0.00094	346.4	200.0	312.2	23.3	309.5	5.8
Bieluagaxi																
BLG1505N-1	63	263	401	0.66	0.05478	0.00381	0.38389	0.02693	0.05086	0.00092	466.7	157.4	329.9	19.8	319.8	5.7
BLG1505N-2	91	410	550	0.75	0.05418	0.00427	0.36719	0.02706	0.05063	0.00101	388.9	177.8	317.6	20.1	318.4	6.2
BLG1505N-3	99	376	582	0.65	0.05297	0.00584	0.38825	0.04180	0.05344	0.00137	327.8	251.8	333.1	30.6	335.6	8.4
BLG1505N-4	61	236	400	0.59	0.05564	0.00468	0.38336	0.02882	0.05228	0.00094	438.9	188.9	329.5	21.2	328.5	5.8
BLG1505N-5	43	186	307	0.60	0.05377	0.00721	0.36715	0.04633	0.05132	0.00142	361.2	302.7	317.5	34.4	322.6	8.7
BLG1505N-6	41	194	323	0.60	0.05373	0.00505	0.37555	0.03618	0.05153	0.00090	361.2	217.6	323.8	26.7	323.9	5.5
BLG1505N-7	58	228	342	0.67	0.05525	0.00775	0.39117	0.05258	0.05377	0.00120	420.4	316.6	335.2	38.4	337.7	7.3
BLG1505N-8	41	198	326	0.61	0.05454	0.00454	0.37109	0.03023	0.05040	0.00091	394.5	187.0	320.5	22.4	317.0	5.6
BLG1505N-9	47	211	331	0.64	0.05337	0.00647	0.39130	0.04507	0.05227	0.00125	346.4	277.7	335.3	32.9	328.4	7.7
BLG1505N-10	47	210	381	0.55	0.05417	0.00500	0.38402	0.03428	0.05208	0.00096	388.9	202.8	330.0	25.2	327.3	5.9
BLG1505N-11	54	245	379	0.65	0.05498	0.00725	0.36582	0.04636	0.05008	0.00128	413.0	298.1	316.6	34.5	315.0	7.9
BLG1505N-12	44	252	347	0.73	0.05533	0.00729	0.38131	0.04782	0.05209	0.00107	433.4	296.3	328.0	35.1	327.4	6.6
BLG1505N-13	24	113	167	0.68	0.04852	0.00832	0.37480	0.06487	0.05105	0.00153	124.2	362.9	323.2	47.9	321.0	9.4
Liushugou																
LSG1501N-1	15	85	100	0.85	0.05535	0.00785	0.37922	0.05527	0.05091	0.00122	427.8	320.3	326.5	40.7	320.1	7.5
LSG1501N-2	25	150	148	1.01	0.05263	0.00789	0.37528	0.05971	0.05043	0.00126	322.3	299.7	323.6	44.1	317.2	7.8
LSG1501N-3	37	233	197	1.18	0.05074	0.00483	0.35928	0.03332	0.04994	0.00084	227.8	207.4	311.7	24.9	314.2	5.2
LSG1501N-4	18	102	142	0.72	0.05371	0.00631	0.36219	0.03945	0.05033	0.00129	366.7	263.9	313.8	29.4	316.6	7.9
LSG1501N-5	24	143	147	0.97	0.05423	0.00616	0.35919	0.04126	0.04988	0.00122	388.9	257.4	311.6	30.8	313.8	7.5
LSG1501N-6	19	104	141	0.74	0.05630	0.00754	0.35368	0.04616	0.04910	0.00132	464.9	272.2	307.5	34.6	309.0	8.1
LSG1501N-7	19	100	117	0.85	0.05915	0.01067	0.36789	0.05573	0.05040	0.00160	572.3	400.0	318.1	41.4	317.0	9.8
LSG1501N-8	36	205	209	0.98	0.05247	0.00423	0.36444	0.02875	0.05035	0.00092	305.6	185.2	315.5	21.4	316.7	5.6
LSG1501N-9	26	157	155	1.01	0.05232	0.00829	0.36672	0.05640	0.04995	0.00146	298.2	335.1	317.2	41.9	314.2	9.0
LSG1501N-10	23	132	157	0.84	0.06908	0.00671	0.46405	0.04112	0.05089	0.00101	901.9	206.5	387.1	28.5	320.0	6.2
LSG1501N-11	27	151	181	0.84	0.05440	0.00512	0.35762	0.03235	0.04925	0.00093	387.1	212.9	310.4	24.2	309.9	5.7

Subducted oceanic slab break-off in a post-collisional setting

Table 2. (*Continued*)

Number	Pb Total ppm	Th 232 ppm	U 238 ppm	Th/U	Isotopic Ratios $^{207}Pb/^{206}Pb$ Ratio	$^{207}Pb/^{206}Pb$ 1sigma	$^{207}Pb/^{235}U$ Ratio	$^{207}Pb/^{235}U$ 1sigma	$^{206}Pb/^{238}U$ Ratio	$^{206}Pb/^{238}U$ 1sigma	Age (Ma) $^{207}Pb/^{206}Pb$ Age (Ma)	$^{207}Pb/^{206}Pb$ 1sigma	$^{207}Pb/^{235}U$ Age (Ma)	$^{207}Pb/^{235}U$ 1sigma	$^{206}Pb/^{238}U$ Age (Ma)	$^{206}Pb/^{238}U$ 1sigma
LSG1501N-12	29	143	137	1.04	0.05478	0.01208	0.36890	0.08724	0.05026	0.00211	466.7	366.3	318.8	64.7	316.1	13.0
LSG1501N-13	41	242	234	1.03	0.05635	0.00567	0.36097	0.03271	0.05003	0.00101	464.9	221.3	312.9	24.4	314.7	6.2
LSG1501N-14	39	234	241	0.97	0.05406	0.00471	0.35498	0.03065	0.04922	0.00085	372.3	200.9	308.5	23.0	309.7	5.2
LSG1501N-15	35	201	186	1.08	0.05469	0.00673	0.35730	0.04373	0.04903	0.00108	398.2	277.7	310.2	32.7	308.6	6.7
LSG1501N-16	19	87	158	0.55	0.05618	0.00862	0.35813	0.05526	0.04907	0.00122	461.2	346.3	310.8	41.3	308.8	7.5
LSG1501N-17	43	242	290	0.83	0.05414	0.00391	0.36117	0.02455	0.04998	0.00089	376.0	162.9	313.1	18.3	314.4	5.5

2009; Tang *et al.*, 2010, 2012b; Yin *et al.* 2010, 2012, 2013, 2015a, 2015b; Li *et al.* 2013, 2015; Gao *et al.* 2014; He *et al.* 2015; Duan *et al.* 2019; Ma *et al.* 2020), the Karamay dykes and host pluton have ages between 298 Ma and 317 Ma, and between 276 Ma and 319 Ma, respectively. The emplacement ages of Xierpu granitoids and dykes range from 298 Ma to 311 Ma and from 299 Ma to 310 Ma, respectively. Bieluagaxi granitoids and dykes have the ages of 299 Ma – 319 Ma and 292 Ma – 324 Ma. Liushugou dykes, intruding into the C_1 strata, have similar age to those of dykes (314 Ma– 321 Ma, Tang *et al.* 2010; An *et al.* 2022a) and plutons (310 Ma – 315Ma) from Baogutu area.

The dykes mostly extend linearly (Fig. 3a, c, e) but some of them are curved or locally deformed (Fig. 3b, d, h). An extensional stress regime is evident due to the irregular jagged contact boundary between dykes and country rocks during the intrusion of these dykes into the pre-existing fractures (Fig. 3b, d, f, h). Thus, based on field observations and petrographic analysis along with geochronological data, we propose that all the dykes were formed after the intrusion of host granitoids, whereas the interval between them is short. When the dykes intruded into the host granitoids, the latter has not been completely cooled and consolidated. This is supported by the proposition that the emplacement interval between the Karamay granitoid and the dykes may have been about one million years (Ma *et al.* 2012).

5.b Petrogenesis of HMA dykes

The studied dykes display similar geochemical features to HMAs with variable SiO_2, MgO and high $Mg^\#$ (Fig. 9b) (Kamei *et al.* 2004). HMAs are generally divided into four types, namely boninite, bajaite, high-Mg adakite and sanukite (Kamei *et al.* 2004). Boninites are characterised by high MgO (>8%) and very low TiO_2 (< 0.5%) (McCarron & Smellie, 1998), which is obviously different from the studied samples. The bajaites have high Sr (>000 ppm) and Ba (>1000 ppm) concentrations, which are also not consistent with our samples (Sr from 294 ppm to 748 ppm; Ba of 358 ppm – 642 ppm with only one sample of 1163 ppm). High-Mg adakites show relatively high SiO_2 (>56%), MgO (< 3%), high $Mg^\#$ values, Sr (>400 ppm), Sr/Y (>40) and $(La/Yb)_N$ (>10) ratios with low Y (<18 ppm) and Yb (<1.8 ppm) (Defant & Drummond, 1990). Sankitoids are characterised by high MgO (generally >5%), $Mg^\#$ (>45) values, high Cr and Ni (both >100 ppm), relatively low Sr and Ba concentrations with low Sr/Y (<40) and $(La/Yb)_N$ (<10) ratios (Kelemen, 1995; Tatsumi, 2006). In the classification diagrams for HMAs, nearly all the dyke samples plot in the field of sanukite (Fig. 8c and d).

Group 1 dykes show relative enrichment of LREEs with fractionated HREE patterns (Fig. 10e), high Sr (564 ppm– 748 ppm) and Sr/Y ratios (40.47–82.85) with low Y (9.03 ppm– 16.8 ppm) and Yb (0.86 ppm–1.67 ppm) concentrations (Table 2). Group 2 samples have similar enrichment of LREEs and fractionated HREE patterns (Fig. 10e), with relatively lower Sr (294 ppm – 618 ppm) and Ba (358 ppm – 503 ppm), and higher Ni (94. 3 ppm – 135 ppm) and Cr (133 ppm – 402 ppm) concentrations (Table 2).

Using data from He (2012) and Chen (2015), along with our new data, Group 2 dykes have higher MgO contents (4.42–8.41, mean value of 7.09, Table 1 and S4) than those of Group 1 (2.56– 6.13, mean value of 4.61, Table 1 and S4), and majority of both groups plot in the high-Mg andesite area with a few samples in the Karamay – Baogutu sanukitoids area (Fig. 9b) except one sample from Karamay area (H8552-1, Table S4). Compared with
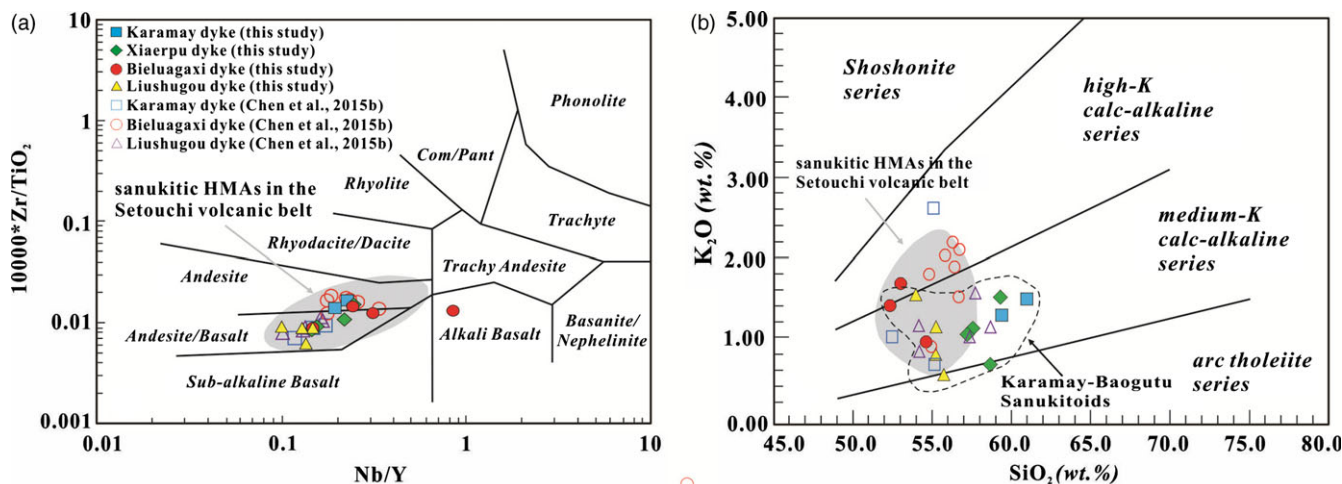
Figure 7. (Colour online) (a) Zr/TiO2 versus Nb/Y and (b) K2O versus SiO2 (Gill, 1981) diagrams. In (a), the data for sanukitic HMAs in the Setouchi volcanic belt are from Shimoda *et al.* (1998), Tatsumi (2001) and references therein.
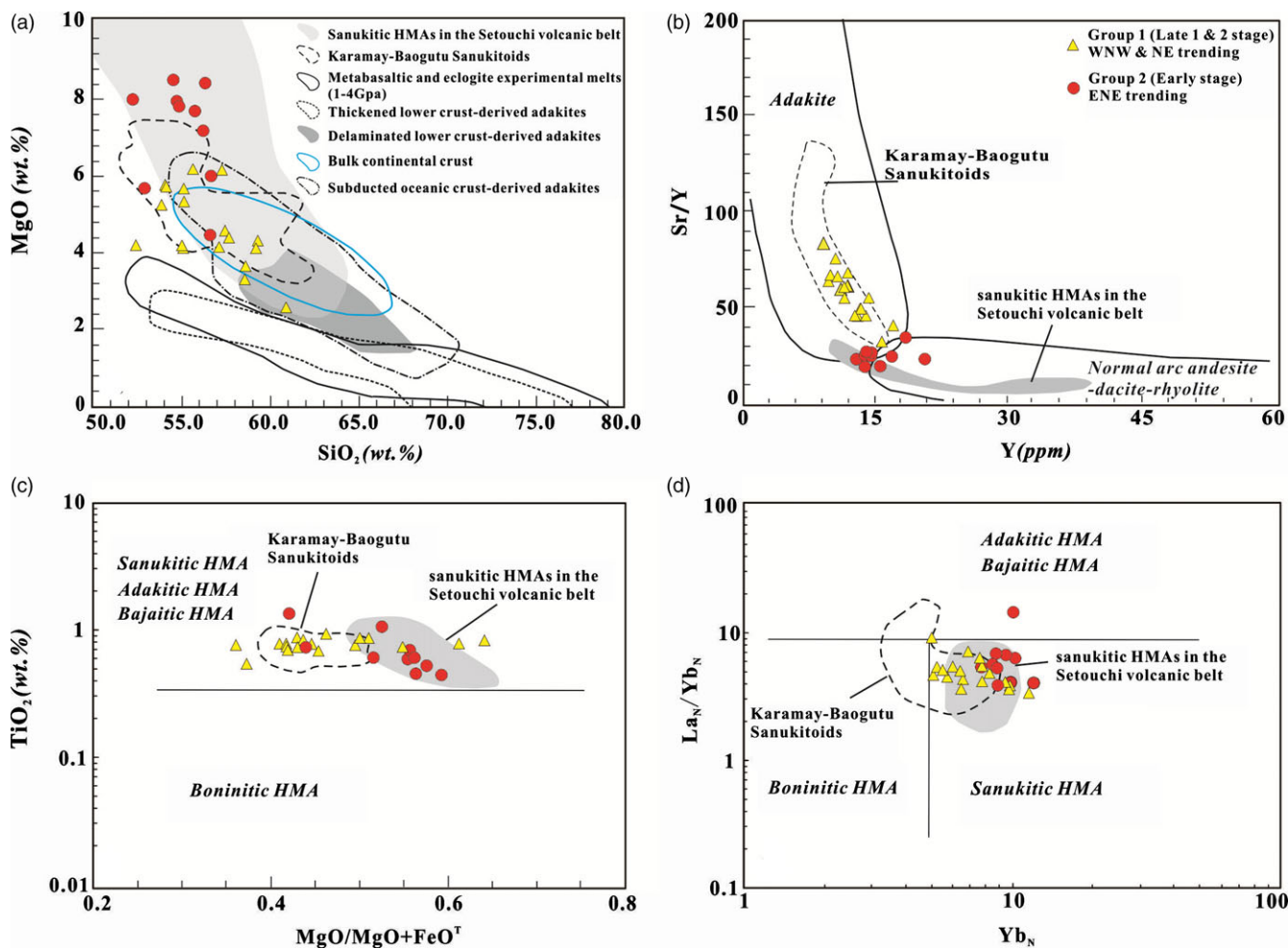

Figure 8. (Colour online) (a) MgO versus SiO2 (McCarro and Smellie, 1998), (b) Sr/Y versus Y diagrams (Defant and Drummond, 1990), (c) TiO2 versus MgO/(MgO+FeOT) (Kamei *et al.* 2004) and (d) LaN/YbN versus YbN (Kamei *et al.* 2004) diagrams. In (a), the field of metabasaltic melts is from Rapp and Watson (1995), and the fields of the subducted oceanic crust-derived, the thickened lower crust-derived adakites are from Wang *et al.* (2011). Sanukitoid data of the Setouchi volcanic belt and Karamay-Baogutu area are from Tatsumi *et al.* (2003), Tang *et al.* (2012a), Ma *et al.* (2012) and Yin *et al.* (2010, 2013), respectively in (a)–(d).
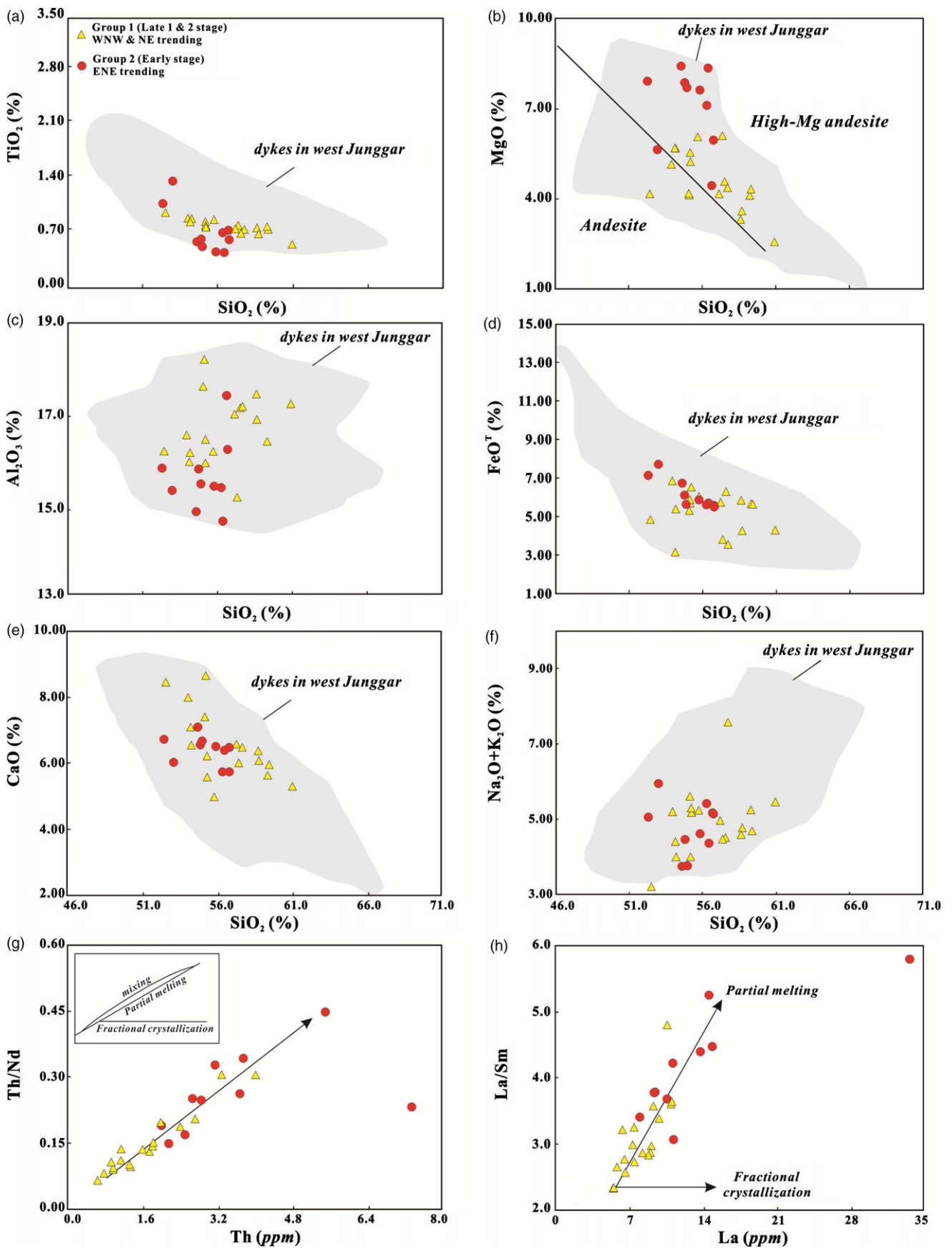
Figure 9. (Colour online) Harker diagrams (a-f), Th/Nd vs. Th (g) (Schiano *et al.* 2010) and La/Sm vs. La (h) (Treuil & Joron, 1975) diagrams for Carboniferous dykes in West Junggar. All the other data refers to Appendix 1 and the data on dykes in West Junggar are from He (2012), Chen (2015), He *et al.* (2015), Ma *et al.* (2012), Tang *et al.* (2012a), Yin *et al.* (2010, 2013, 2015a, 2015b) and Zhang and Zou, (2013). Trace plots for the discrimination of partial melting, fractional crystallisation and magma mixing in (g) are from (Schiano *et al.* 2010).
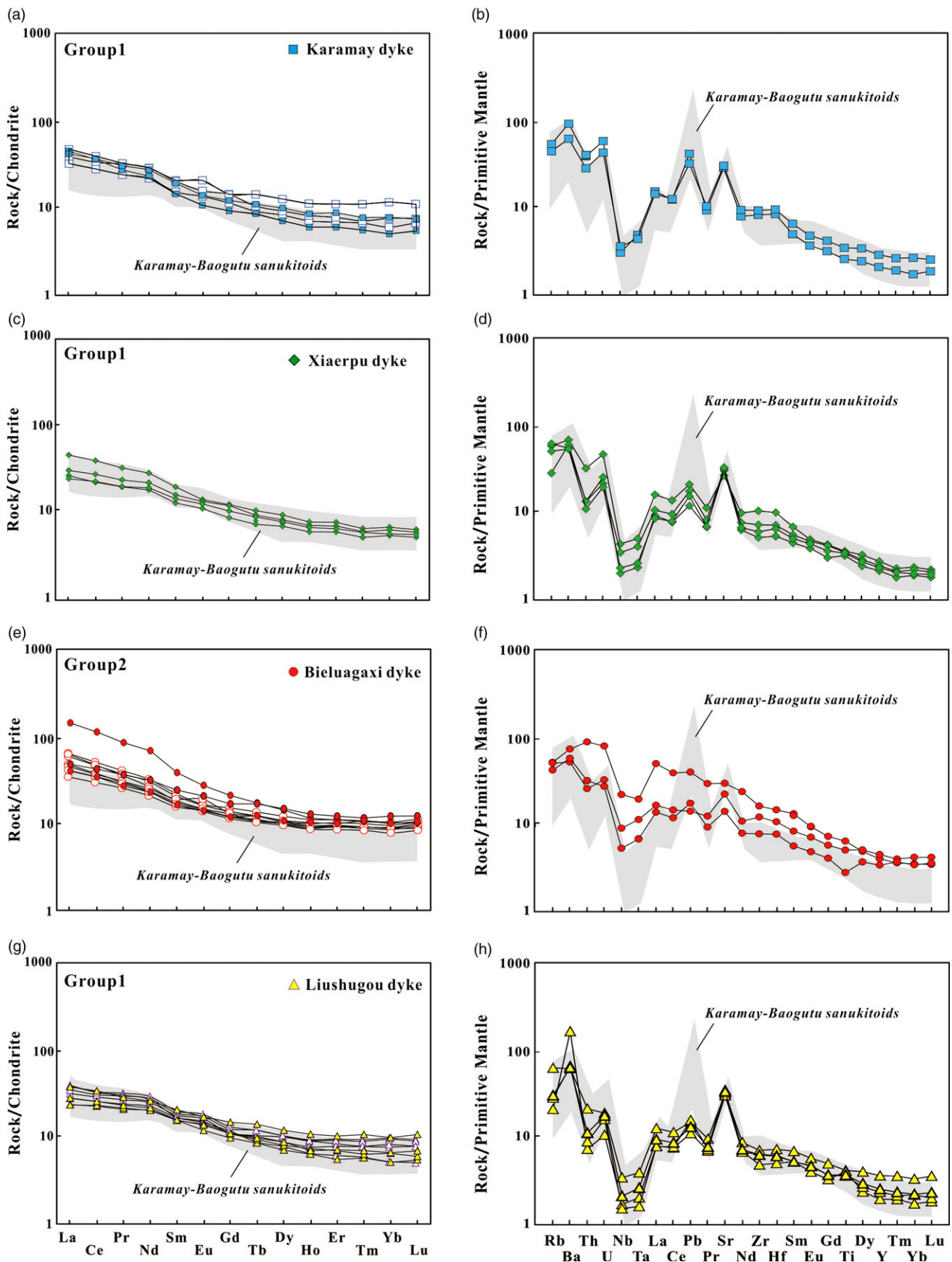
Figure 10. (Colour online) Chondrite-normalised rare earth element diagram (a, c, e and g) and primitive mantle-normalised trace-element variation diagram (b, d, f and h) of dykes in West Junggar. Chondrite, Primitive mantle, MORB and OIB data are from Sun and McDonough (1989). The Karamay-Baogutu area is from Tang *et al.* (2012a), Ma *et al.* (2012) and Yin *et al.* (2010, 2013).

geochemical characteristics of high-Mg adakites and sanukitoids, Group 1 is similar to Karamay-Baogutu sanukitoids [these are widespread in Karamay – Baogutu area in central West Junggar and show similar geochemical features to sanukitic rocks with low $(La/Yb)_N$ ratios but classify as adakites field with high Sr/Y ratios, Yin *et al.* (2010, 2013); Ma *et al.* (2012)], and Group 2 shows similarities to sanukitoids.

5.b.1 Crustal contamination and fractional crystallisation

Despite some compositional differences observed among various dykes in both groups of samples, they share relatively similar low initial $({}^{87}Sr/{}^{86}Sr)_i$ ratios and high positive $\varepsilon Nd(t)$ values (Table 3; Fig. 11a). The Nb/La and $({}^{87}Sr/{}^{86}Sr)_i$ ratios are essentially constant with increasing $Mg^{\#}$ and SiO_2 (Fig. 12a and b), which rules out significant crustal contamination during magma ascent and emplacement. This interpretation is also consistent with the lack of significant correlation between Nb/La and Sm/Nd (Figure not shown).

The negative correlations of TiO_2, FeO^T, MgO and CaO with SiO_2, for the two groups of dykes (Fig. 9a, b, d and e), indicate fractional crystallisation of olivine and pyroxene. There is no obvious correlation between Al_2O_3, total alkalis and silica (Fig. 9f). The trace element variation in these dykes, when combined with data from other reported dykes in West Junggar, also suggests that fractional crystallisation of olivine and orthopyroxene has taken place (Fig. 12d), which is consistent with the presence of hornblende + biotite as the dominant mafic minerals/phenocrysts in the rocks (Fig. 4a, c, e, f and h). The Cr and Ni abundances of Group 1 dykes can be quantitatively explained by the 0–18% fractionation of 95% orthopyroxene and 5% olivine (Fig. 12d) starting from the assumed parent magma composition represented by the relatively least fractionated sample H8747-5 from Group 1 samples. The quantitative simulation of the Cr and Ni abundances from Group 2 samples could be derived from 0 to 10% fractionation of 75% orthopyroxene and 25% olivine starting from the assumed parent magma composition represented by the least fractionated sample BLG1505h (Fig. 12d). The noticeable positive Sr anomalies and negligible negative Eu anomalies demonstrate that plagioclase was not a major fractionating phase in either group (Fig. 10). The positive linear correlation in the $(La/Yb)_N$ ratios vs. La diagram (Fig. 12e) for the Liushugou and Xiaerpu dykes suggests that the 0–0.02% fractional crystallisation of apatite could explain the composition of Group 1 samples (Fig. 12e, f). Modelling suggests that the Karamay samples in Group 1 experienced 0–0.02% fractional crystallisation of zircon (Fig. 12e, and g). Group 2 samples experienced fractional crystallisation of 0–0.05% monazite starting from the assumed parent magma composition represented by the least fractionated sample BLG1505h.

5.b.2 Petrogenesis of Group 1 dykes

The Group 1 dykes in West Junggar also have high $Mg^{\#}$ values, Ni and Cr concentrations, indicating that they are likely to be melts derived from the mantle (Rapp & Watson, 1995). They have relatively low $({}^{87}Sr/{}^{86}Sr)_i$ (0.7035–0.7044) and slightly high $\varepsilon Nd(t)$ values (+4.5–+7.8), which are similar to the granitoids and dykes, which are derived from partial melting of the basement (i.e., subducted and trapped juvenile oceanic crust, Xu *et al.* 2013; Gao *et al.* 2014; Zhang *et al.* 2018; Zheng *et al.* 2020) in West Junggar (Fig. 11a; Table S5). The Group 1 dykes have high Th/La and low Nb/Th ratios that plot in the compositional spectrum of forearc basalts, indicating an oceanic slab-related origin (Fig. 14e) and this

Table 3. Sr-Nd isotopic data of the Late Carboniferous dykes in West Junggar

Sample No.	Age (Ma)	Rb (ppm)	Sr (ppm)	${}^{87}Rb/{}^{86}Sr$	${}^{87}Sr/{}^{86}Sr$	2s	$({}^{87}Sr/{}^{86}Sr)_i$	Sm (ppm)	Nd (ppm)	${}^{147}Sm/{}^{144}Nd$	${}^{143}Nd/{}^{144}Nd$	2s	T_{DM} (Ga)	T_{DM2} (Ga)	εNd
KM1503h	311.3	11.9	313.14	0.1099	0.703985	0.0013	0.70349	6.11	24.09	0.1532	0.512945	0.0007	0.521	0.450	7.75
KM1510h	311.3	24.09	601.6	0.1158	0.704388	0.0013	0.70387	2.76	12.33	0.1187					
XP1505h	309.7	11.54	654.38	0.051	0.704077	0.0011	0.70385	2.58	11.07	0.1408	0.512757	0.0006	0.825	0.712	4.54
XP1507h	309.7	16.14	519.69	0.0898	0.704105	0.0014	0.70371	2.6	10.9	0.1442	0.512888	0.0009	0.578	0.511	6.96
BLG1502h	324.3	11.07	404.78	0.0791	0.704793	0.0012	0.70443	6.5	36.86	0.1066	0.51267	0.0006	0.686	0.726	4.36
BLG1505h	324.3	6.56	343	0.0553	0.704385	0.0014	0.70413	5.17	26.34	0.1187	0.512765	0.0005	0.621	0.619	5.65
LSG1501h	313.9	18.68	519.34	0.104	0.70481	0.0013	0.70435	2.86	12.06	0.1436	0.512796	0.0006	0.773	0.660	5.22
LSG1505h	313.9	13.88	609.89	0.0658	0.704074	0.0013	0.70378	2.18	9.31	0.1419	0.512903	0.0007	0.528	0.479	7.37
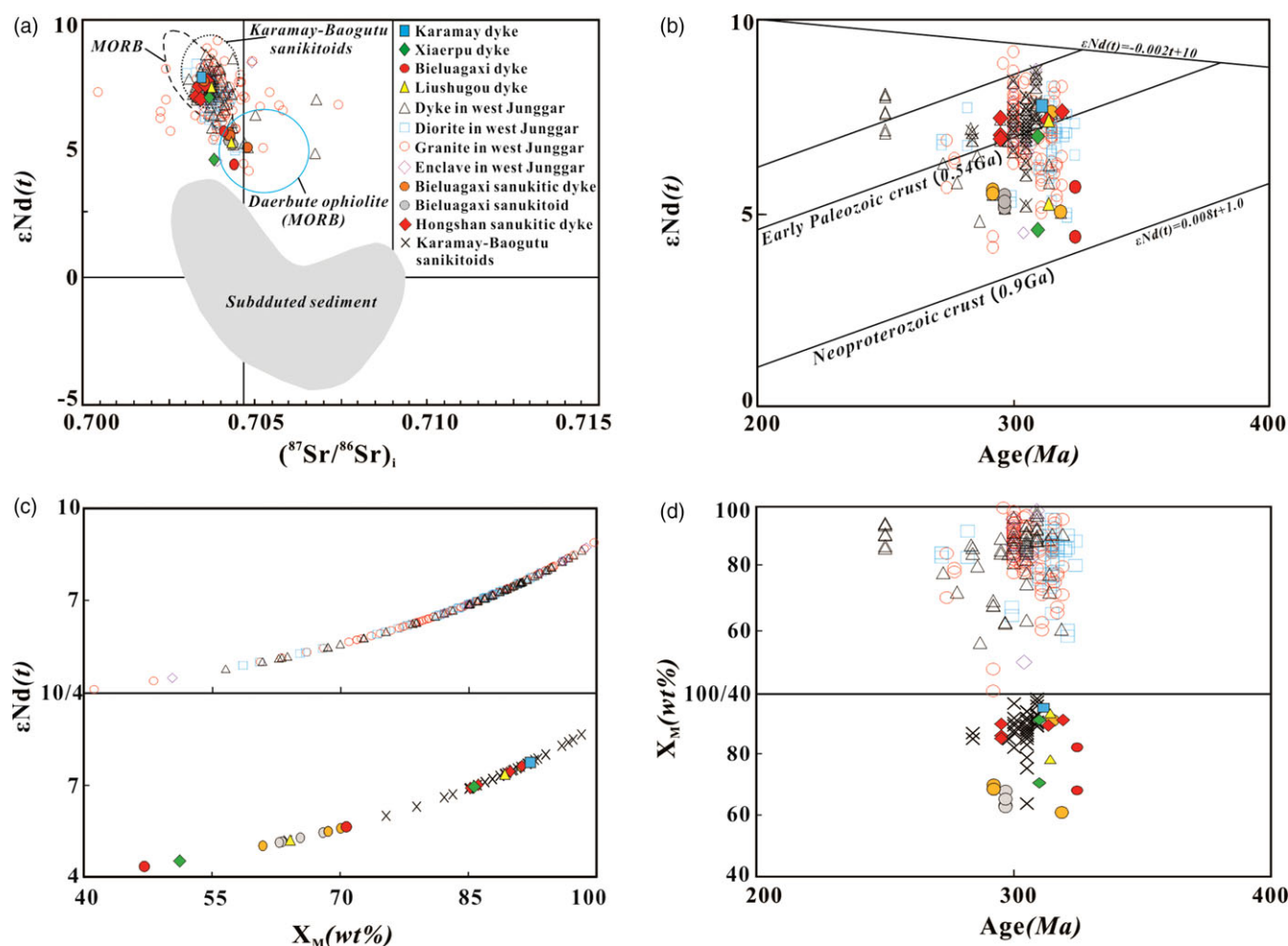
Figure 11. (Colour online) εNd(t) versus (87Sr/86Sr) i (a), εNd(t) versus age (b), estimated proportion of mantle-derived materials in magmatic rocks based on Nd isotope two-end member mixing calculation (c) and estimated mantle proportion versus age of the igneous rocks in Central West Junggar (d). The Sr-Nd isotopic data of granite and diorite in West Junggar are from Geng *et al.* (2009), Tang *et al.* (2012b), Xu *et al.* (2013), Gao *et al.* (2014), Yin *et al.* (2015a), Li *et al.* (2015), Liu *et al.* (2017) and Zheng *et al.* (2020); the Sr-Nd isotopic data of dykes in West Junggar are from Yin *et al.* (2010, 2012, 2012, 2013, 2015a, 2015b), Tang *et al.* (2010, 2012a, 2012b), Ma *et al.* (2012), Xu *et al.* (2013), He *et al.* (2015), Li *et al.* (2015), Zhan *et al.* (2015), Duan *et al.* (2019) and Ma *et al.* (2020). The Sanukitoid data of the Karamay-Baogutu area are from Tang *et al.* (2012a), Ma *et al.* (2012) and Yin *et al.* (2010, 2013). In (d) and (e), the number represents the fractionated number. In (f)–(h), F is fractionated number. Partition coefficients are from Rollinson (1993), Green and Pearson (1986), Mahood and Hildreth (1983) and Yurimoto *et al.* (1990). Abbreviations: Ol = olivine, Opx = orthopyroxene, Cpx = clinopyroxene, Hb = hornblende, Ap = apatite, Mon = monazite, Allan = allanite.

is also consistent with high Th/Yb ratios relative to Mid Ocean Ridge Basalt (MORB) (Fig. 14f). All of these features indicate an oceanic crust source and their young Nd model ages (T_{DM}) prove that their source is juvenile.

High magnesium magmas can be generated by the partial melting of hydrous peridotite mantles (Hirose, 1997), particularly when hydrous felsic liquids from the subducting oceanic slab or sediment-derived melts trigger partial melting (Mukasa *et al.* 2007). In a subduction zone, Sr and Ba are mobile in aqueous fluids, while LREE and Th are preferentially transferred from the slab when sediment-derived melts are involved. Therefore, ratios such as Ba/La, Th/La, Th/Yb and Sr/Yb can be used to assess the influence of aqueous fluids and sediment-derived melts (Johnson & Plank, 1999). Apart from Liushugou dykes with variable Ba/La ratios suggesting that their generation was related to the oceanic-slab-derived fluid, Group 1 dykes have high Th/Yb but low Ba/La ratios (e.g., Fig. 14a), indicating that sediment-derived melt plays a dominant role in the formation of most dykes in West Junggar. However, the magmatic zircons in both groups of dykes have

moderate U/Yb ratios and Y contents (Fig. 12c), which are consistent with both continental zircon and ocean crust zircon (Grimes *et al.* 2007). In Fig. 14b, c and d, the samples plot on a trend between GLOSS or sediment and MORB, indicating interaction between peridotite mantle and sediment-derived melt.

The retention of zircons in the sedimentary residue would result in significant depletion of Zr and Hf in the resultant magmas (Woodland *et al.* 2018). Both groups of samples do not show negative Zr-Hf anomalies on primitive mantle-normalised diagrams (Fig. 10b, d, f and h), indicating no or few residual zircons and a high degree of sediments melting. Furthermore, the presence of broad or weak zoning in the CL images of both group dykes indicates that the zircons in these rocks crystallised from high-temperature melts (Fig. 5; Wu & Zheng., 2004), which is also confirmed by the crystallisation temperatures (Table S6) of the magmatic zircons (estimated by using the Ti-in-zircon thermometry, Ferry & Watson, 2007). Karamay, Xiaerpu and Liushugou dykes (Group 1) have crystallisation temperatures of 789 °C–940 °C, 804 °C–1006 °C and 772 °C–1112 °C.
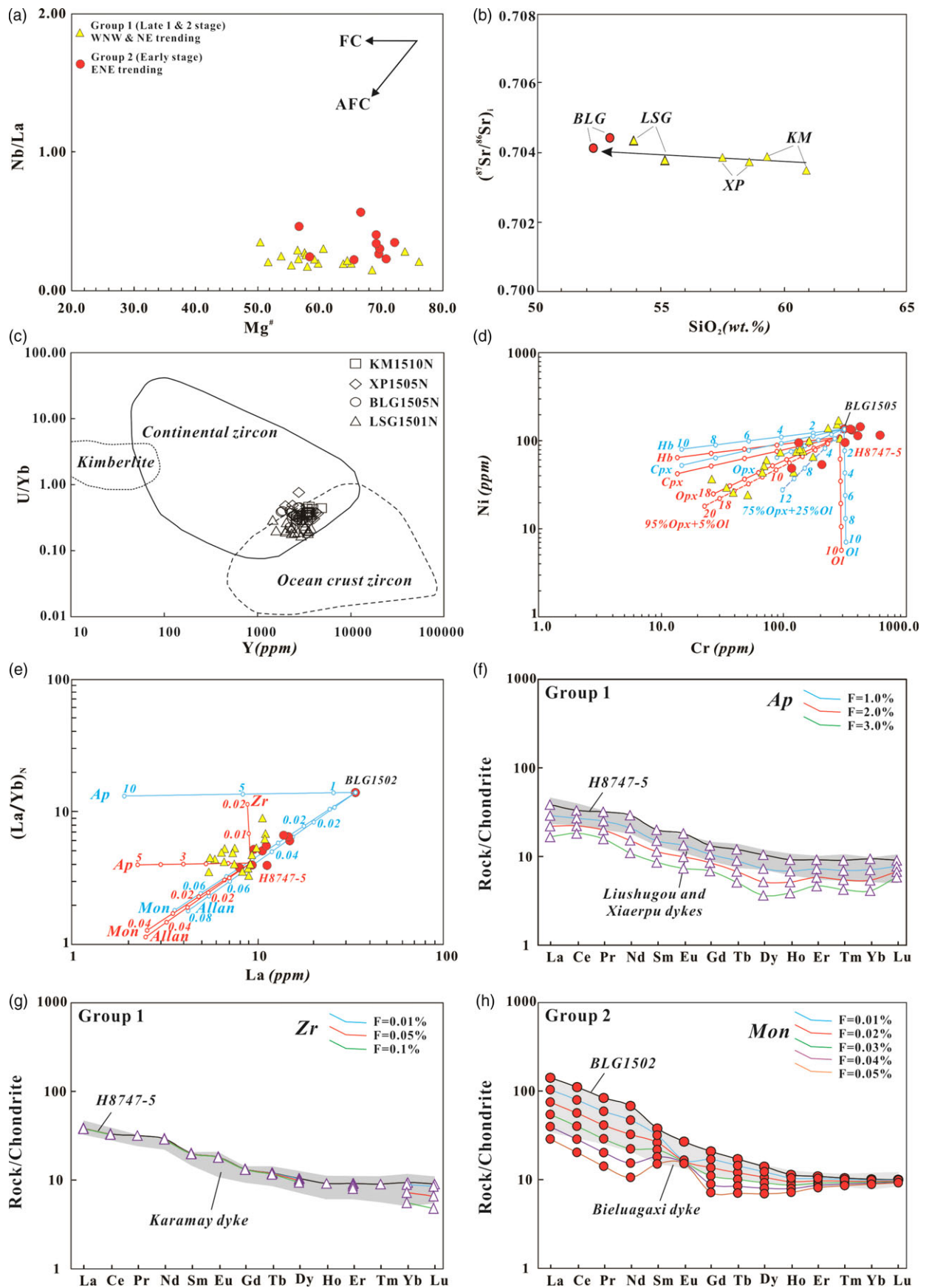
Figure 12. (Colour online) Nb/La versus Mg# (a) (He *et al.* 2009), (87Sr/86Sr)i versus SiO2 (b), U/Yb versus Y (c) (Grimes *et al.* 2007), modelled Ni versus Cr (d), modelled (La/Yb) N versus La (e) and the rare earth elements changes with different degree of apatite fractionated of Group 1 Liushugou and Xiaerpu dykes in Group 1 (f), zircon fractionated of Group 1 Karamay dykes (g), and monazite fractionated of Group 2 Bieluagaxi dykes (h).
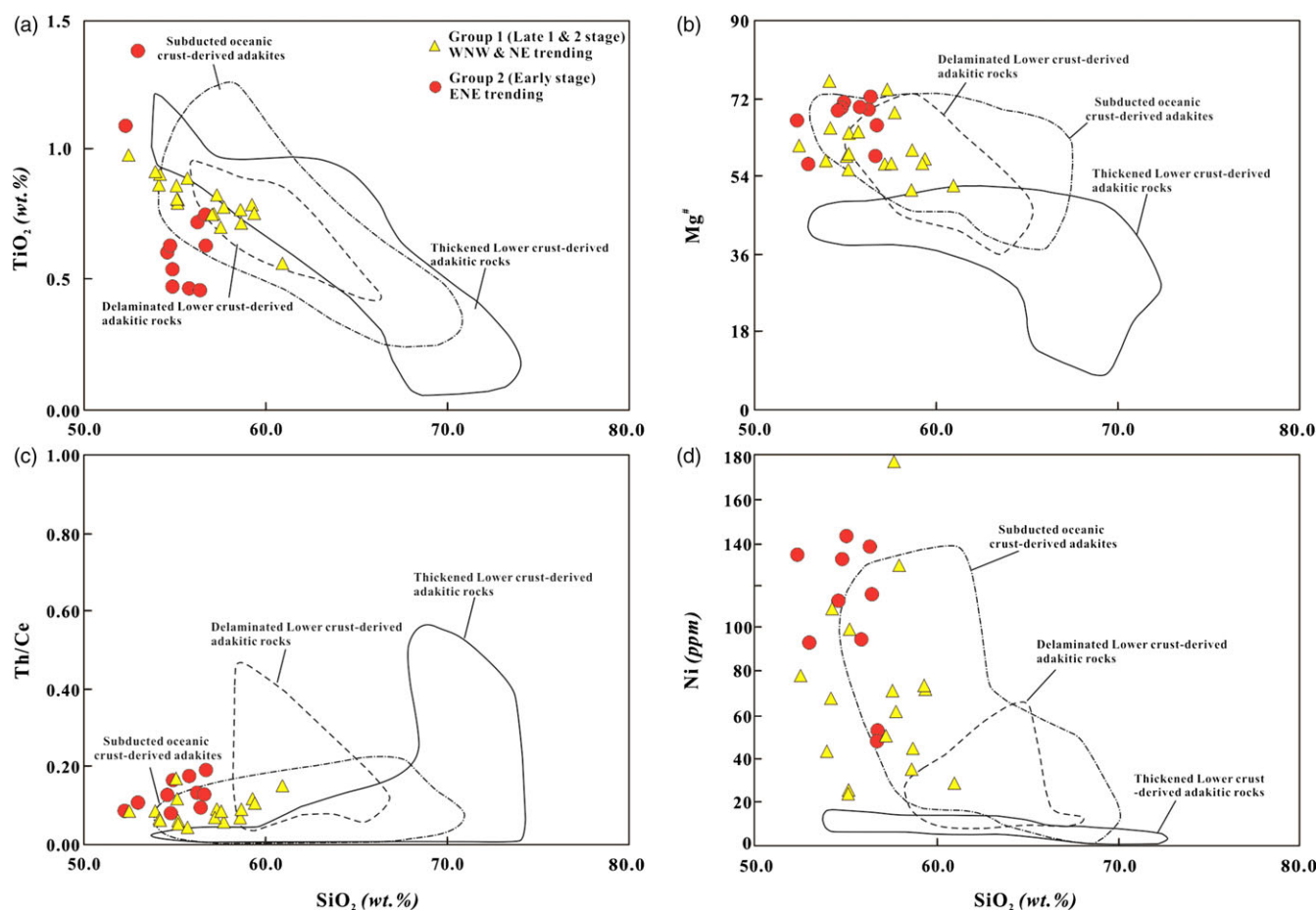
Figure 13. (Colour online) TiO2 vs. SiO2 (a), Mg# vs. SiO2 (b), Th/Ce vs. SiO2 (c) and Ni vs. SiO2 (d) diagrams. Fields of subducted oceanic crust-derived adakites, thick lower crust-derived adakitic-like rocks and delaminated lower crust-derived adakitic-like rocks are after Wang *et al.* (2006).

Several models have been proposed to explain the relatively high Sr/Y ratios and Mg# values of the HMAs, including (1) magma mixing with subsequent contamination (Guo *et al.* 2007); (2) fractional crystallisation of mantle-derived basaltic magma (Li *et al.* 2009, 2013); and (3) melt–mantle interaction (Chung *et al.* 2003; Gao *et al.* 2004; Martin *et al.* 2005). Group 1 dykes have relatively similar low initial (^{87}Sr/^{86}Sr)$_i$ ratios and high positive εNd(*t*) values (Table 3; Fig. 11a), which precludes the possibility of crustal contamination. Geochemical modelling of batch partial melting, fractional crystallisation and magma mixing can be used to investigate the processes that exert an influence on the trace-element variations of cogenetic magmas (Schiano *et al.* 2010). Modelling of partial melting and fractional crystallisation would produce a straight line with a slope and a horizontal line, respectively, in plots of two incompatible elements with different partition coefficients (e.g., Th/Nd vs. Th, La/Sm vs. La; Fig. 9g and h) (Treuil and Joron, 1975; Schiano *et al.* 2010). These plots of the Group 1 dykes show that they could have been generated by partial melting rather than fractional crystallisation or magma mixing (Fig. 9g and h). Hence, the model (1) and (2) can be ruled out. This conclusion is also supported by geological and geochemical observations, including (1) the general absence of mafic magmatism in central West Junggar during the Late Carboniferous – Early Permian. Therefore, fractional crystallisation cannot account for the widespread coeval intermediate to felsic magmas; (2) the lack of disequilibrium texture of phenocrysts

and the presence of compositional ortho-zonal structure in plagioclase phenocrysts in the Group 1 dykes suggest that there has not been extensive magma mixing; (3) The Mg# of these high-Mg rocks are comparable to those of crust-derived melts that underwent assimilation with peridotite in the mantle (Fig. 13b; Rapp *et al.* 1999). (4) The dykes coexist with Nb-enriched-like rocks in central West Junggar, which are generally considered to be produced by the melting of mantle metasomatized by slab-derived melts (Yin *et al.* 2013).

There are three mechanisms for melt–mantle interaction between peridotite mantle and the (1) subducting oceanic slab-derived melt (e.g., Defant & Drummond, 1990); (2) delaminated lower crust-derived melt (e.g., Gao *et al.* 2004); or (3) thickened lower crust-derived melt (e.g., Wang *et al.* 2006). The subducting slab-derived melt and subsequent interaction with mantle is preferred based on the following lines of evidence: (1) The major and trace-element compositions of the West Junggar dykes fit well within the fields of subducting oceanic slab (Figs. 8a, and 12). They have high MgO, Mg#, Ni and Cr contents, which resemble those of subducting oceanic slab-derived adakitic-like rocks (Defant & Drummond, 1990). They have low TiO2 (0.56 %–0.98 %), Mg# values (52–76), Th/Ce (0.05–0.17) ratios and high but variable Ni contents (24 ppm – 178 ppm), which are similar to subducted slab-derived adakitic melts (Fig. 13) but distinct from the thickened or delaminated lower crust-derived adakitic rocks (Chung *et al.* 2003; Wang *et al.* 2006). (2) Their REE and trace-element patterns
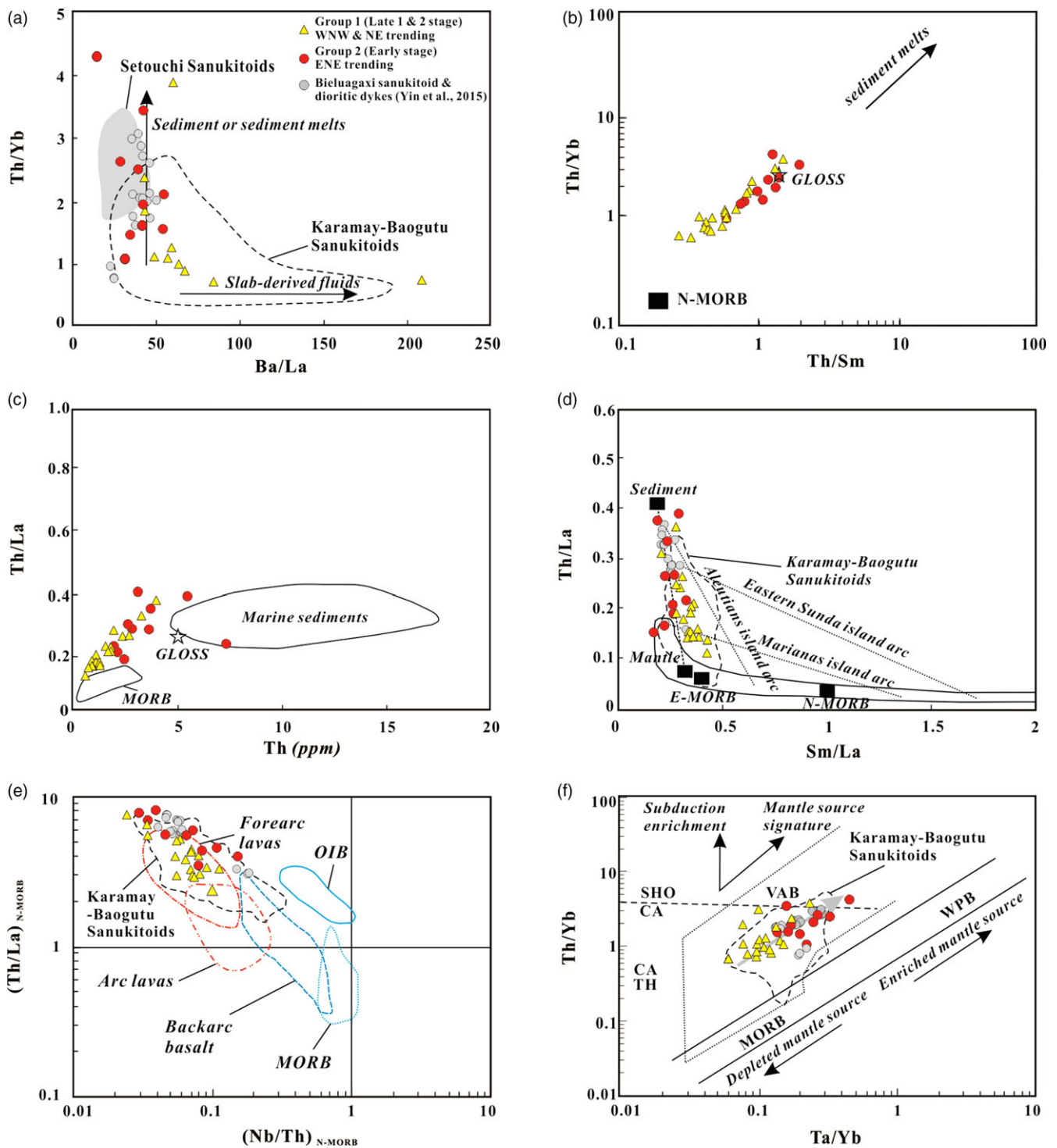
Figure 14. (Colour online) Th/Yb versus Ba/La (a) (Woodhead *et al.* 2001), and Th/Yb versus Th/Sm (b) (Liu *et al.* 2021), Th/La versus Th (c) (Plank and Langmuir, 1998), Th/La versus Sm/La (d) (Plank, 2005), Normal-MORB (Sun & McDonough, 1989) normalised plots of (Th/La) N-MORB versus Nb/Th N-MORB (e) (Liu *et al.* 2014) and Th/Yb versus Ta/Yb (f) (Pearce, 1982) diagrams of the Carboniferous dykes in West Junggar. The trace-element data are from He, 2012, Ma *et al.* 2012, Tang *et al.* 2012a, Chen, 2015, He *et al.* 2015 and Yin *et al.* 2010, 2012, 2013, 2015a, 2015b. In (a), the sanukitic data of Setouchi volcanic belt are from Tatsumi (2003). In (d)–(f), the Sanukitoid data of the Karamay-Baogutu area are from Tang *et al.* (2012a), Ma *et al.* (2012) and Yin *et al.* (2010, 2013). The data of EMORB, N-MORB and Mantle are from Sun and McDonough (1989), and the GLOSS is referred by Plank and Langmuir (1998).

are similar to those of the adakitic – like Karamay – Baogutu saukitoids, which are widely considered to be derived from the reaction between subducting oceanic slab and the peridotite mantle (Fig. 10) (Yin *et al.* 2010, 2013); (3) However, mechanisms involving over-thickened and delaminated lower crust are not

favoured by their high positive εNd values (+4.54 – +7.75). (4) Group 1 dykes have rather high Sr concentrations (491 ppm–789 ppm) with mean value of 660 ppm, which indicates that the mantle was probably metasomatized by the melts (Martin *et al.* 2005).
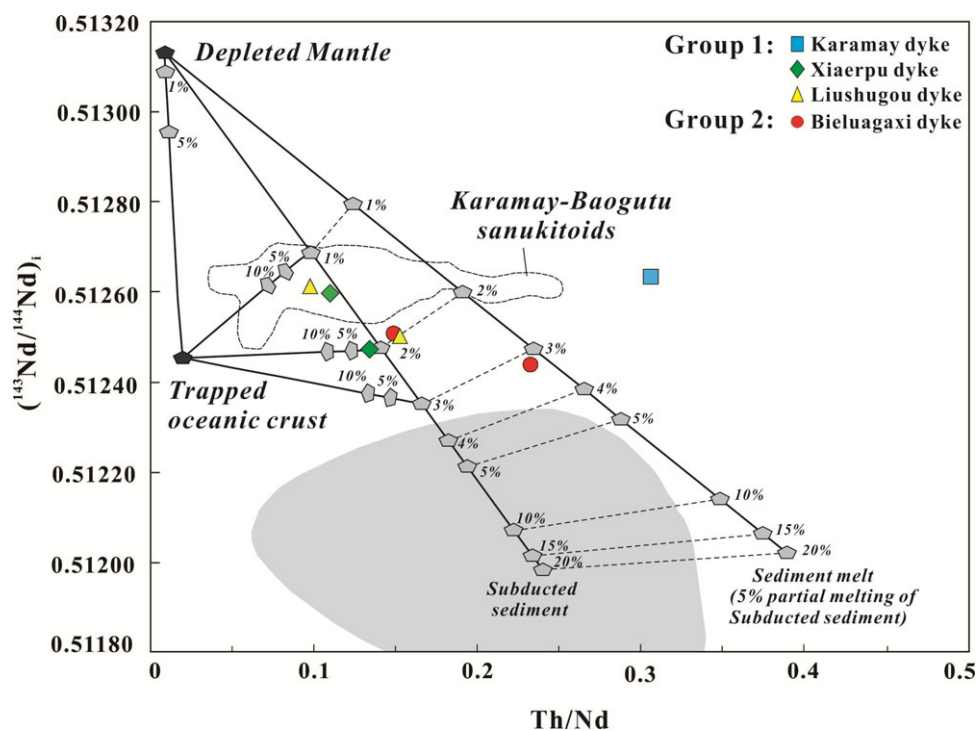
Figure 15. (Colour online) Plot of Th/Nd versus 143Nd/144Nd(t) of the Carboniferous dykes in west Junggar. Subducted sediment from Plank *et al.* (2007), Plank and Langmuir (1998), Nowell *et al.* (1998) and Vervoort *et al.* (2011). DMM trace-element concentrations are from Su and Langmuir (2003) and Workman and Hart (2005). Sediment/melt and sediment/fluid partition coefficients from Johnson and Plank (1999). The trapped oceanic crust was represented by klm28 (metagabbro) from Zhu *et al.* (2015). The Sanukitoid data of the Karamay-Baogutu area are from Tang *et al.* (2012a), Ma *et al.* (2012) and Yin *et al.* (2010, 2013).

A plot of Th/Nd ratio vs. (^{143}Nd/^{144}Nd)$_i$/εNd(t) (Johnson & Plank, 1999; Zhang *et al.* 2021b) can be used to model the contribution of sediment-derived melt and three-component mixing models (DePaolo *et al.* 1991) for the dykes are shown Fig. 15. This modelling shows that 1%–2% sediment/sediment partial melt and 0–5% trapped oceanic crust-derived melts mixed with a depleted mantle source could generate the compositions of the Group 1 dykes (Fig. 15).

The presence of residual accessory phases profoundly controls the trace-element composition of the adakitic melts. Therefore several characteristic trace-element concentrations and ratios are commonly regarded as proxies for residual accessory phases in magma sources and so can be used to evaluate the pressure and temperature conditions of melting. The Sr/Y and (La/Yb)$_N$ ratios of intermediate-felsic magmas are essentially controlled by the mineral phases (e.g., garnet, rutile, amphibole and plagioclase) in the residue or by fractionation crystallisation of parent magma. Group 1 dykes have relatively steep HREE patterns ((Gd/Yb)$_N$ = 1.24–2.26 mean value of 1.66) with high Sr/Y (31.68–82.85, mean value of 56.26) ratios, which are similar to the Karamay-Baogutu sanukitoids ((Gd/Yb)$_N$ = 1.11–2.56; Sr/Y = 26.18–129.53 mean value of 52) (Table S4), which were derived from a source containing some residual garnet and rutile (Yin *et al.* 2010, 2013; Ma *et al.* 2012; Tang *et al.* 2012a). However, Group 1 dykes show Nb-Ta negative anomalies but without distinct Ti depletion on a primitive mantle-normalised multi-element plot (Fig. 10b, d and h), suggesting that rutile is absent in the magma source. Ratios such as K/Yb and Dy/Yb can be used to distinguish between melting in the spinel and garnet stability field of phlogopite- and/or amphibole-bearing lherzolite (Duggen *et al.* 2005) because melting in the spinel

and garnet stability field would produce melts with low Dy/Yb ratios (<1.5) and high Dy/Yb ratios (>2.5), respectively. Group 1 samples have Dy/Yb ratios of 1.60–2.24, indicating that they were probably derived from melting of a source in the spinel-garnet transition zone. As plagioclase is not a major fractionation phase and garnet is a residual in the source with fractionation of orthopyroxene and olive (Fig. 12d), Group 1 dykes have relatively high Sr/Y ratios. However, compared with typical adakitic rocks, the Group 1 dykes have low (La/Yb)$_N$ ratios, which was most likely caused by partial melting of peridotite mantle metasomatized by oceanic slab-derived adakitic melts (Ma *et al.* 2012; Yin *et al.* 2013). This indicates that the melt-mantle interaction may have diluted their adakitic features (Fan *et al.* 2020). Based on a minimum pressure (1.5GPa) for rutile appearance, the depth for Group 1 sample production via melting of subducted oceanic crust cannot exceed 50 km (Xiong *et al.* 2005; Xiong, 2006). Using MORB as a source rock, phase-equilibrium modelling indicates that adakites are generated under P-T conditions of 1.0–1.6 GPa and 800–1000 °C (Wang et al, 2020). Thus, it is clear that Group 1 dykes were formed at relatively high-temperatures (800°C–1050°C) and relatively high-pressure conditions (<1.5 Gpa) (Defant & Drummond, 1990; Xiong, 2006; Yin *et al.* 2013).

5.b.3 Petrogenesis of Group 2 dykes

The Group 2 dykes have similar characteristics of high Mg$^{\#}$ values, Ni and Cr concentrations, relatively low (^{87}Sr/^{86}Sr)$_i$ (0.7041–0.7044) and high εNd(t) values (+4.4–+5.7) to the Group 1 dykes, indicating that they are derived from depleted mantle (Rapp & Watson, 1995). They have high Th/La and low Nb/Th ratios, and plot in the forearc basalts area, suggesting an oceanic slab-related

origin (Fig. 14e). Their high Th/Yb ratios relative to MORB (Fig. 14f), positive high εNd(t) values and young Nd model ages (T_{DM}) indicate a juvenile depleted mantle source. Three main models for the formation of sanukitic HMAs in the Setouchi volcanic belt have been suggested: (1) Peridotite mantle assimilated by the intermediate-felsic magma (i.e., TTG-like melts) at crustal depths in intra-continental setting (Qian & Hermann, 2010). (2) Remelting of mantle-wedge peridotite modified by interaction with aqueous fluids derived from slab dehydration (Tatsumi & Hanyu, 2003) or (3) subducting sediments (Shimoda *et al.* 1998; Tatsumi & Hanyu, 2003).

In relation to model (1), Qian and Hermann (2010) proposed that intermediate-felsic magmas were formed in an extensional setting by partial melting of lower crust followed by reaction of this melt with peridotite at middle or upper crustal levels. Petrographic observations and geochemical compositions of Group 2 samples (Figs. 4 and 9) differ from those HMAs generated by model 1, which usually comprise a certain amount of olivine xenocrysts or dunite xenoliths and display adakitic-like compositions with high Sr, Ba but strong Nb-Ta depletions (Qian & Hermann, 2010). Furthermore, there is no evidence in the area for the emplacement of peridotite at middle or upper crustal levels, and thus this model does not represent a feasible mechanism for the generation of the West Junggar dykes.

We propose that Group 2 dykes were derived from remelting of mantle-wedge peridotite modified by interaction with subducting sediments rather than aqueous fluids based on following evidence: (1) They possess high MgO, Mg#, Ni and Cr contents than typical island-arc andesites (Tatsumi, 2006). (2) On the MgO vs. SiO_2 diagram (Fig. 8a), Group 2 samples show similarities to sanukitic HMAs in the Setouchi volcanic belt (Tatsumi, 2001; Yin *et al.* 2015), not only reflecting the differences in initial compositions compared with Group 1 samples but also suggesting a similar formation mechanism to Setouchi sanukitoids, which were generated by interaction between the peridotite mantle and sediment-derived melt in a young, or hot, subduction zone setting (Furukawa & Tatsumi, 1999). (3) The concentration of Th in marine sediments is more than two orders of magnitude higher than that of the mantle, and therefore the addition of sediment to the mantle will lead to increasing Th/La, Th/Sm and Th/Y ratios and decreasing (Nb/Th) ratios but will have little effect on Ta/Yb ratios (Plank & Langmuir, 1998; Liu *et al.* 2014). Group 2 have high Th/Yb and low Ba/La ratios, suggesting that they were generated by partial melting of the peridotite mantle metasomatized by sediment-derived melts, which is supported by the fact that they plot along a mixing line between the mantle and sediments on a Th/La vs. Sm/La, Th/La vs. Th and Th/Yb vs. Th/Sm and $(Th/La)_{N-MORB}$ vs. $(Nb/Th)_{N-MORB}$ diagrams, further suggesting significant interaction between subducting sediments and peridotite mantle (Fig. 14b, c and d). This depleted source had possibly undergone metasomatic enrichment by sediment-derived melt, resulting in an enriched-LILE and depleted-HFSE signature (Fig. 10e, f). (4) Fig. 15 indicates that addition of 2%–3.5% sediment/sediment partial melt to depleted mantle can model the composition of sanukitic Group 2 dykes in central West Junggar (Johnson & Plank, 1999; Zhang *et al.* 2021b).

Group 2 samples have Dy/Yb ratios of 1.61–2.08, indicating that like Group 1 dykes they were probably derived from melting of a source in the spinel-garnet transition zone. In Fig. 9d, Group 2 samples show no obvious Ti depletion indicating that rutile is not the residual phase. They have relatively flat HREE patterns ((Gd/Yb)$_N$ = 1.19 – 1.50 with mean value of 1.47 (Fig. 10e), low Sr/Y

ratios of 18.67 – 33.9 (mean value of 24.07) and relatively low (La/Yb)$_N$ ratios, suggesting that there was little residual garnet in their source region. Moderate Y/Yb and (Ho/Yb)$_N$ ratios indicate that the residual phase in the source region of Group 2 samples is mainly amphibole rather than garnet (Wu *et al.* 2002). They display noticeable positive Sr anomalies and negligible negative Eu anomalies demonstrating that plagioclase was a residue in the source region (Fig. 10e, f). The phase-equilibrium between the melts and the plagioclase and amphibole during the partial melting of the basalts constrained by experimental petrology indicates that they were formed at pressures lower than 0.8 GPa (Ge *et al.* 2002; Wu *et al.* 2002). The Bieluagaxi dykes (Group 2) give Ti-in-zircon crystallisation temperatures between 783°C and 1013°C (Ferry & Watson, 2007), which is similar to the crystallisation temperatures of the Group 1 samples.

Thus, Group 2 dykes were most likely derived from partial melting of peridotite mantle metasomatized by sediment-derived melts at a shallow depth but relatively high temperatures.

5.c Tectonic setting

Widespread Cambrian-Ordovician ophiolites and overlying Ordovician-Silurian volcanic-sedimentary rocks in Northern Xinjiang indicate that an early Palaeozoic Junggar Ocean existed in this region (Xu *et al.* 2013). The age span of ophiolites or ophiolitic mélanges in West Junggar ranges from 572±25 Ma to 332±14 Ma (Zhang *et al.* 2018 and references therein). Daerbute and Karamay ophiolitic mélanges in central West Junggar (Fig. 2) are thought to be formed in a subduction-related setting from 426 Ma to 375 Ma (Chen & Zhu, 2011; Yang *et al.* 2012b) and from 414 Ma to 363 Ma, respectively (Xu *et al.* 2006; Yang *et al.* 2013). In addition to the ophiolite complexes and mélanges, this subduction in the Early Carboniferous is evidenced by granitoids (e.g., Han *et al.* 2006), dyke swarms (e.g., Tang *et al.* 2012a) and volcanic rocks (e.g., Geng *et al.* 2011), which have island arc signatures (Feng *et al.* 1989; Xiao *et al.* 2008).

Various tectonic settings of West Junggar in Late Carboniferous have been proposed from post-collisional (Chen & Arakawa, 2005; Han *et al.* 2006; Chen *et al.* 2010; Xu *et al.* 2013; Gao *et al.* 2014; Zheng *et al.* 2020), to subduction-accretionary (Windley *et al.* 2007; Xiao *et al.* 2008) to ridge subduction settings (Geng *et al.* 2009; Tang *et al.* 2010, 2012a; Ma *et al.* 2012; Yin *et al.* 2010, 2013, 2015a). Arc magmatism ceased at the beginning of Late Carboniferous and the wide spatial distribution of granitoids formed in West Junggar during Late Carboniferous – Early Permian does not fit with the narrow and linear distribution pattern of magmatism that would be expected if slab break-off had occurred (Whalen *et al.* 2006; Li *et al.* 2015). Both group dykes are characterised by enrichment in LILEs and depletion in HFSEs and significant negative Nb anomaly showed by the two groups of dykes (Fig. 9) reveals that they may have been formed in a subduction-related setting (Rudnick & Gao, 2003) (Fig. 10). However, no record of oceanic crust and accretion-collision processes or (ultra-)high-pressure metamorphism younger than 300 Ma have been reported, indicating that the subduction-related setting is not a good choice (Liu *et al.* 2019). Thus, based on following pieces of evidence, we propose a post-collisional setting in West Junggar since Late Carboniferous:

(1) Choulet *et al.* (2012) argued that accretion and subduction in the West Junggar must have ceased during the Late Carboniferous with transition from an accretionary to a post-accretionary setting between 305 Ma – 300 Ma, which is consistent
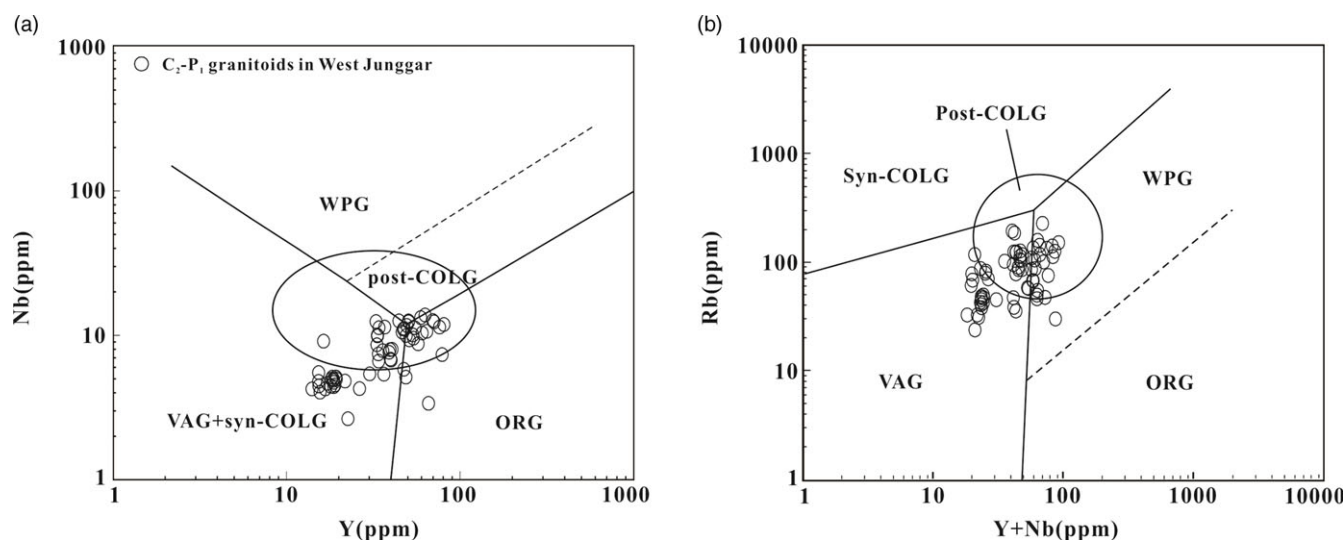
Figure 16. Tectonic discrimination diagrams of (a) Nb vs. Yb (Pearce *et al.* 1984) and (b) Rb vs. Y+Nb (Whalen *et al.* 1987). ORG, ocean-ridge granites; post-COLG, post-collision granites; syn-COLG, syn-collision granites; VAG, volcanic arc granites; WPG, within-plate granites. All the data of Late Carboniferous to Early Permian granitoids are listed in Table S7 from Gao *et al.* (2014) and references therein.

with the lack of evidence for Permian subduction in the sedimentary or tectonic records (Buckman & Aitchison, 2004; Choulet *et al.* 2012). (2) Early Carboniferous magmatism has been ascribed to this subduction-accretion event, which then developed into an intra-continental orogenic event both in the northern and southern West Junggar region during the late Early Carboniferous to the early Late Carboniferous (Duan *et al.* 2019). (3) Late Carboniferous collisional events between different tectonic blocks (e.g., Yili-Chinese central Tianshan block and Junggar terrane along the Chinese north Tianshan suture zone) (Zhang *et al.* 2016; Han & Zhao, 2018) in northern Xinjiang, led to the closure of the West Junggar remnant ocean basin and other sub-oceans of the Palaeo-Asian Ocean (Han & Zhao, 2018). The final closure of the Junggar Ocean likely occurred at the end of the Late Carboniferous in response to regional amalgamation events in the southwestern CAOB, representing the final assembly of the Kazakhstan Orocline (Zhang *et al.* 2021a). (4) Undeformed mafic – intermediate dykes dissect the deformation structures including folds and faults, which were correlated with subduction-accretionary process in Early Carboniferous, present that the cessation of subduction-accretionary process when the abundances of dykes were emplaced (Zhan *et al.* 2015). Because these dykes could be deemed as 'stitching rocks', they were formed after the deformation caused by subduction-accretionary process in Early Carboniferous. (5) Stress measurements on the studied dykes (172 in total) were obtained during field work and calculated by method from Delvaux and Spencer (2003). All dykes were formed in an extensional stress regime including pure, oblique and strike-slip extensional regimes (Table S8). This is consistent with the conclusion that the mafic – intermediate dykes in West Junggar formed in within-plate extensional setting, coeval with the widespread lithospheric extensional events in the Northern Xinjiang (Coleman, 1989; Jahn *et al.* 2000; Han *et al.* 2006; Zhan *et al.* 2015). (6) Widespread deposition of Permian continental molasse deposits followed the formation of post-collisional magmatic rocks (Zong *et al.* 2016). The Gzhelian Molaoba Formation consisting of non-marine fluvial sediments represents the central West Junggar back-arc basin that finally closed by the Late Carboniferous (Liu *et al.* 2017). (7) Abundances of Late Carboniferous – Early Permian

undeformed A-type granitic intrusions in West Junggar (emplacement ages between 305 Ma and 280 Ma) have highly-depleted Hf-Nd isotopic affinities. They have been proposed to be derived from depleted mantle or juvenile basaltic lower crust that was generated in an extensional post-collisional setting (e.g., Xu *et al.* 2013; Gao *et al.* 2014; Zheng *et al.* 2020). Minor contemporaneous I-type granites were derived from the differentiated products of the basaltic melts or a mixture between basaltic melts and juvenile lower crust (Chen *et al.* 2010). The Late Carboniferous – Permian granitoids in West Junggar (Table S7) are plotted in the VAG and Post-COLG settings, which show transitional affinities (Fig. 16). They were probably formed in a transitional background from subductional to post-collisional settings. Additionally, the dykes were generated a little later than the host granitoids, indicating that they were probably formed in a post-collisional setting.

5.d Magmatic flow and emplacement of dykes

5.d.1 Magmatic flow of dykes
Syn-tectonic magmatic flow is defined as deformation by melt displacement with consequent rigid-body crystal rotation, but without sufficient interference between crystals to cause plastic deformation (Paterson *et al.* 1989). Although flow structures in dykes and plutons are generally seldom observed at outcrop or under the microscope, they include alignment of bubbles or phenocrysts in dykes, orientation and strain of enclaves, hot striations on the contact, magmatic foliation or lineation in plutons, rarely ropy flow structure and other structures (Baer, 1987; Tian & Shan, 2011; Zhou & Wang, 2012). All above are useful to determine the flow direction of magma, thus helping understand the processes responsible for magma mixing or segregation during flow, nucleation and propagation of dykes.

Flow structures observed in Bieluagaxi dykes rather than other dykes in West Junggar are mainly magmatic bands and folds. These structures were produced in the magma body as a result of flow-induced shearing within the dykes. In outcrop, the magmatic bands appear dark grey or light white in colour, with a variable amount of euhedral or subhedral hornblende and plagioclase

and/or quartz crystals of several millimetres in diameter. They are generally parallel or subparallel to the boundaries of dykes (Fig. 3i and j) but are not always parallel to each other, and they sometimes may make up rootless isocline folds (Fig. 3j). The contact between the bands and their ambient rocks is straight, slightly undulating or occasionally zigzag (Fig. 3i and j). As distinguishing the folding mechanisms is difficult or even impossible due to the insufficient observations at most outcrops, we just describe two interesting types: injection folds and disharmonic folds. The former appears at the blunt end of the dyke (Fig. 3j). Generally, they are isoclinal with the axial plane oriented parallel or subparallel to the sides of dykes. However, in the Fig. 3j, this injection fold occurs in local part of the dyke. The disharmonic fold has a variable size and thickness with respect to the limbs (Fig. 3h). Neither foliation nor cleavage is visible in the cores of this tight fold, suggesting the disturbance of flow-induced shearing by continuous laminar flow after magmatic bands formed in dykes.

In this study, the magmatic banding is generally considered a product of magma mingling due to the fact that most of the bands are parallel or subparallel to the contact. The megacryst K-feldspar has poikilotopic texture that euhedral amphiboles and acicular apatites embedded in the plagioclase (Fig. 4g), which is also supported by the plagioclase xenocrysts (Fig. 3g), dioritic xenolith (Fig. 3h) and round-to-elongated-shaped granitic enclaves (Fig. 3k) in dykes, indicating that the magma of the dioritic dyke was initially quenched into the unconsolidated host granitic magma and mingled with it to a certain extent.

5.d.2 Emplacement of dykes

The strike and dip orientation analysis of the dyke swarm confirms the prevalence of sub-vertical and sub-horizontal WNW-trending dykes (Late 1 stage) with minor NE- (Late 2 stage) and ENE-trending (Early stage) dykes throughout the entire study area (Fig. 2, S2; Table S1). The WNW- and NE-trending sub-vertical and sub-horizontal dyke orientation and ENE-trending (Early stage) sub-vertical dyke orientation appear to coincide with one of the two main fracture sets (NE-SW and WNW-ENE) in the host rocks (Fig. 3a, c, S3c, e, i and j) in Karamay, Xiaerpu and Bieluagaxi areas, and with localised NE-ENE-trending fractures or faults in Liushugou area (Fig. 3e, S3k), respectively, a fact that is compatible with the possibilities that most dykes could have exploited pre-existing joints/faults or that dykes and dyke/parallel joints/faults are contemporaneous.

Variations in strike and/or dip have also been observed along individual dykes, revealing a continuous zigzagging stepped geometry (Fig. 3a, S3c, e, g–i) and are probably equally related to the exploitation of joints (Martinez-Poza & Druguet, 2016). The joints/faults within the host granitic rocks and surrounding Upper Carboniferous strata were generated in an extensional regime in Late Carboniferous. The joints/faults show tensile characteristics in the field (Fig. S3b, f, g, h and j). Thus, the tensile joints/fractures of the host granitic rocks and surrounding strata were formed in that extensional setting in Late Carboniferous, immediately or in a very short time after being filled by magma propagation. As discussed in section 5.d.1, the magmas of dioritic dyke were initially quenched into the unconsolidated host granitic magma, indicating that the emplacement interval between the dykes and host granites may have been very short, which is also indicated by their similar ages. In other words, these pre-existing joints/fractures were formed after the emplacement of granitoids in a tensional regime in Late Carboniferous, and the time interval between these pre-existing joints/fractures and dykes may be probably only a few

million years. Thus, these joints/fractures could be deemed as the 'contemporaneous' products with dykes in central West Junggar. A plausible model is that 'contemporaneous' joints in the granitoids were exploited during dyke emplacement and subsequently reactivated during cooling and post-cooling events, implying active tectonics during and after the intrusion of the dyke swarm (Martinez-Poza & Druguet, 2016).

The dykes are parallel and they were formed in response to the regional tensile stress field (Hou, 2012). Our paleostress analysis gives an estimation of the orientation and relative magnitude of the tectonic principal stress axes operating at the time of intrusion (Fig. S2). To Karamay and Bieluagaxi dykes, the $\sigma 1$ was sub-vertical, and $\sigma 2$ and $\sigma 3$ sub-horizontal, whereas the $\sigma 2$ of the dykes in Xiaerpu and Liushugou areas were sub-vertical with $\sigma 1$ and $\sigma 3$ sub-horizontal (Table S8; Fig. S2). There is a good correspondence between these paleostress values and field structures observed between dyke patterns in horizontal and vertical sections. Emplacement of the dykes took place in the form of extension fractures during a regional extensional tectonic regime with strike-slip, as inferred from the sub-vertical and sub-horizontal principal stress axes ($\sigma 1$). Dykes preferentially opened perpendicular to their walls. The estimated average extension (T) accommodated by dyke intrusion is considerable as 2.7% (Li *et al.* 2005). Numerous dyke swarms, found in West Junggar, show similar geochemical and isotopic affinities of a post-collisional setting in Late Carboniferous. It is therefore likely that there is a magma chamber of relevant components in the deep part of the dyke.

Thus, the dyke intrusion extensional seems to have been favoured by the presence of 'contemporaneous' joints or fractures/faults in the host granitic rocks or strata. The final pattern of dykes likely resulted from the interaction between these fractures and the external tectonic stress tensor active during dyke emplacement.

5.e Tectonic implications

In West Junggar, a Late Carboniferous magmatic association of various volcanic and intrusive rocks is extensively developed and is mostly derived from a mantle magmatic source (Chen & Jahn, 2004; Geng *et al.* 2009; Chen *et al.* 2010; Yin *et al.* 2010; Zheng *et al.* 2020). Late Carboniferous (306 Ma – 315 Ma) N-MORB to OIB-like tholeiitic and alkaline basalts in Yeyagou, Maliya and Hatu were discovered and interpreted as derived from various enriched mantle sources (Zhang et al, 2011a, 2011b) or from a mixed mantle source consisting of subducted depleted oceanic lithosphere and enriched upwelling asthenospheric mantle associated with ridge-trench interaction (Tang *et al.* 2012c). However, recent work has shown that the Junggar basin is composed of (1) an assemblage of Late Palaeozoic arc fragments, accretionary complexes and trapped oceanic crust (Li *et al.* 2015), or (2) oceanic crust (Xu *et al.* 2013) consistent with the idea that the basement of the West Junggar region is mainly composed of slices of oceanic crust (Zheng *et al.* 2007; Zhang *et al.* 2018) with minor Precambrian basement (Hu *et al.* 2000). Existing geophysical data show that the Junggar Basin is characterised by high velocity, density and magnetisation (Zhao *et al.* 2008). A preserved Palaeo-oceanic lithosphere, which is becoming a piece of Eurasian continent beneath the Junggar region, has been presented by seismic evidence (Wu *et al.* 2023), which suggests that the basement of the Junggar Basin is oceanic crust.

Post-collisional magmatism was triggered by asthenosphere upwelling resulting in the widespread formation of Late Carboniferous and Permian granitoids and dykes in West Junggar and adjacent regions, e.g., Altay, Tianshan and North Tianshan

(Han *et al.* 2006; Zheng *et al.* 2020). This interpretation is supported by Sr-Nd isotopic signatures of the magmatic rocks in West Junggar, which show widespread development of juvenile crust with minimal contribution of Precambrian rocks that preclude the occurrence of TTG (Zheng *et al.* 2020). The generation of the HMAs needs high-temperature conditions to trigger partial melting of the subducted slab and sediments (Tatsumi, 2008). Considering the occurrence of high Sr/Y type HMAs and sanukitic dykes with those tholeiitic and alkaline basalts in West Junggar, they are not only the indicator of an extensional setting but also a high-temperature geothermal gradient. Unlike Archean HMAs, commonly considered to be produced at a very high geothermal gradient (Martin *et al.* 2005), the Phanerozoic HMAs such as the Late Carboniferous sanukitic dykes in West Junggar require special dynamic processes to elevate the geothermal gradient of the post-Archean upper mantle (Shimoda *et al.* 1998).

There are two possible tectonic scenarios for raising the geothermal gradient, i.e., lithospheric delamination or subducted slab break-off (Liu *et al.* 2017). Both processes may result in asthenosphere upwelling and coeval basaltic underplating, leading to the partial melting of oceanic crust. Delamination may produce non-linear diffuse distribution of magmatism in a large area, whereas the magmatism caused by slab break-off will be confined to a narrow linear zone with significant crustal uplift (Whalen *et al.* 2006; Liu *et al.* 2017). The spatial-temporal pattern of Carboniferous magmatism in West Junggar shows a tendency to southward-younging in West Junggar (Zhang *et al.* 2021a), which makes slab break-off model more feasible. This suggestion is also consistent with the uplift of the Junggar terrane remnant oceanic crust during its final development between 335 Ma and 333 Ma (Zhu *et al.* 2015). The Late Carboniferous adakitic rocks and HMA-like rocks from the Karamay and Baogutu region could also be produced by partial melting of the broken-off oceanic crust during the initial phase of orogenic collapse (Ren, 2013).

In the Early Carboniferous, the back-arc basin, which resulted from northwest-ward intra-oceanic subduction of the Junggar Ocean in the Zhongguai area between the Junggar complex basement and the Yili block (Zhang *et al.* 2018), started to subduct with generation of arc-related I-type granites. Numerous volcano-clastic and tuffaceous materials from Carboniferous arc-related rocks were deposited quickly in this back-arc basin (Zhang *et al.* 2021a). During subduction, the oceanic slab underwent break-off resulting in asthenosphere upwelling and the tectonic regime changed from compression to an extensional post-collisional setting in the early Late Carboniferous. The trapped oceanic-crust-like basement of West Junggar was heated by the asthenospheric mantle and began to melt. Thus, Bieluagaxi (324 Ma) dykes derived from the reaction between the peridotite mantle and the sediment-derived melts at a shallow depth but low temperature.

Magmatic activity mostly occurred between ca. 332 Ma and 287 Ma based on the systematic combining and summarising of available zircon U-Pb chronological data of granitoids in West Junggar (Duan *et al.* 2019). During this period, the magmatism was successive and showed two important phases of magmatic activities with peak ages of ca. 314 Ma and ca. 302 Ma. During this period, many magmatic rocks including A-type granites, adakitic-like and sanukitic-like rocks with minor tholeiitic, alkaline and Nb-enriched-like rocks were produced during the mantle-crust interaction process in the post-collisional regime. In Late Carboniferous, the slab-derived melt with adakitic affinity interacted with peridotite mantle and sediment-derived melts resulting in the formation of Group 1 dykes along the joints and

fractures to transport and propagate. The Carboniferous strata were then folded during the tectonic extrusion of the Daerbute and Karamay ophiolitic mélanges because the central West Junggar terrane, which was situated in the core area of the Kazakhstan Orocline, underwent tectonic uplift and extensive deformation (Zhang *et al.* 2018).

5.f Phanerozoic Continental crustal growth

The Canadian – Alaskan Cordillera of North America and the CAOB are two large Phanerozoic orogenic belts that contain significant accounts of juvenile materials (Patchett & Samson, 2003). The CAOB was built by the subduction and closure of the Palaeo-Asian Ocean and is surrounded by the Siberian craton to the north, and the Tarim and North China cratons to the south and the European craton to the west (Zheng *et al.* 2020). The West Junggar orogenic belt is correlated with arc-related magmatism and accretion of oceanic rocks from latest Ediacaran to Early Carboniferous and was associated with asthenosphere upwelling-related magmatism in post-collisional setting during Late Carboniferous to Permian (Gao *et al.* 2014; Zheng *et al.* 2020).

In West Junggar, widespread Late Carboniferous – Early Permian magmatism is mostly characterised by primitive $\varepsilon Hf(t)$ and $\varepsilon Nd(t)$ values and Palaeozoic model ages, which indicate massive continental crust growth by recycling of oceanic crust or direct differentiation of basaltic underplated material that originated from melting of a metasomatized lithospheric mantle (Jahn *et al.* 2000; Han *et al.* 2006; Chen *et al.* 2015). It has been estimated that nearly 50% of the continental crust in the CAOB is juvenile and the granitoids (Table S7) with high positive $\varepsilon Nd(t)$ values contain more than 50% mantle-derived or juvenile materials (Sengör *et al.* 1993; Jahn *et al.* 2000). The estimate of the proportion of depleted mantle in the mixture can be semi-quantified by using a simple two-end member mixing model (DePaolo *et al.* 1991). The majority of granitoids, dykes and enclaves in West Junggar plot between the crust and depleted mantle, and rocks with similar ages show approximately vertical trends, suggesting variable mixing of the crust and the depleted mantle (Fig. 11a and b) with large proportions of mantle components (Fig. 11c and d). The mantle components in Late Carboniferous igneous rocks including granitoids, dykes and enclaves in central West Junggar vary from 41.2% to 99.7% with average value of 84.6% (Fig. 9c and d). These post-collisional igneous rocks including studied samples with Sr-Nd isotopes characterised by young T_{DM} and high positive $\varepsilon Nd(t)$ values suggest considerable continental crustal growth in a post-collisional setting during Late Carboniferous to Early Permian.

6. Conclusions

(1) LA-ICP-MS zircon U-Pb dating results reveal that the dykes in central West Junggar were formed between 309.7±2.4 Ma and 324.3±3.6 Ma and show coeval relationships with their corresponding host rocks.

(2) The dykes are divided into two groups based on Sr/Y ratios: Group 1 including Karamay, Xiaerpu and Liushugou dykes with high Sr/Y ratios of 41–83, which are similar to the adakitic HMA; whereas Group 2 includes Bieluagaxi dykes with low Sr/Y ratios of 19–34, which resemble the sanukitic HMA.

(3) It is proposed that 1%–2% sediment/sediment partial melt and 0–5% trapped oceanic crust-derived melts mixed with a

depleted mantle source could generate the compositions of the adakitic-like Group 1 dykes, and 2%–3.5% sediment/ sediment partial melt interacting with the depleted mantle may form the sanukitic Group 2 dykes in West Junggar.
(4) Large-scale asthenosphere upwelling could explain much of the magmatism and substantial continental crustal growth of West Junggar in the Late Carboniferous-Early Permian.

References

An F, Zhu YF, Lehmann B, Zheng B and Qiang JL (2022a) The Baogutu gold deposit in west Junggar, NW China: an epizonal intrusion-related gold deposit. *Ore Geology Reviews* **150**, 105188.

An F, Zhu YF, Wei SN, Zhang H and Zhao L (2022b) Variation of crustal thickness in central west Junggar orogenic belt: insight into its Late Palaeozoic tectonic evolution. *International Geology Review* **64**, 1799–816.

BGMRX (1993) *Regional Geology of Xinjiang Uygur Autonomous Region.* Beijing: Geological Publishing House, 841 (in Chinese).

Buckman S and Aitchison JC (2004) Tectonic evolution of Palaeozoic terranes in West Junggar, Xinjiang, NW China. *Geological Society of London, Special Publication* **226**, 101–29.

Chen B and Arakawa Y (2005) Elemental and Nd-Sr isotopic geochemistry of granitoids from the West Junggar foldbelt (NW China), with implications for Phanerozoic continental growth. *Geochimica et Cosmochimica Acta* **69**, 1307–20.

Chen B and Jahn BM (2004) Genesis of post-collisional granitoids and basement nature of the Junggar Terrane, NW China: Nd-Sr isotope and trace element evidence. *Journal of Asian Earth Sciences* **23**, 691–703.

Chen B and Zhu YF (2011) Petrology, Geochemistry and zircon U-Pb chronology of gabbro in Darbut ophiolitic melange, Xinjiang. *Acta Petrologica Sinica* **27**, 1746–58 (in Chinese with English abstract).

Chen JF, Han BF, Ji JQ, Zhang L, Xu Z, He GQ and Wang T (2010) Zircon U-Pb ages and tectonic implications of Paleozoic plutons in northern West Junggar, North Xinjiang, China. *Lithos* **115**, 137–52.

Chen JF, Han BF, Zhang L, Xu Z, Liu JL, Qu WJ, Li C, Yang JH and Yang YH (2015) Middle Paleozoic initial amalgamation and crustal growth in the West Junggar (NW China): constraints from geochronology, geochemistry and Sr-Nd-Hf-Os isotopes of calc-alkaline intrusions in the Xiemisitai-Saier Mountains. *Journal of Asian Earth Sciences* **113**, 90–109.

Chen XJ (2015) The characteristics and the geodynamic background of the dyke system in Houshan areas of Karamay, western Junggar, NW China. MSc Dissertation. China University of Geosciences, Wuhan, 64–76.

Choulet F, Faure M, Cluzel D, Chen Y, Lin W and Wang B (2012) From oblique accretion to transpression in the evolution of the Altaid collage: new insights from West Junggar, northwestern China. *Gondwana Research* **21**, 530–47.

Chung SL, Liu DY, Ji JQ, Chu MF, Lee HY, Wen DJ, Lo CH, Lee TY, Qian Q and Zhang Q (2003) Adakites from continental collision zones: melting of thickened lower crust beneath southern Tibet. *Geology* **31**, 1021–4.

Coleman RG (1989) Continental growth of Northwest China. *Tectonics* **8**, 621–35.

Defant MJ and Drummond MS (1990) Derivation of some modern arc magmas by melting of young subducted lithosphere. *Nature* **347**, 662–5.

Delvaux D and Sperner B (2003) New aspects of tectonic stress inversion with reference to the TENSOR program. In *New Insights into Structural Interpretation and Modelling* (ed DA Nieuwland), 75–100: Geological Society, London, Special Publication, 212.

DePaolo DJ, Linn AM and Schubert G (1991) The continental crust age distribution: methods of determining mantle separation ages from Sm–Nd isotopic data and implication to the southwestern United States. *Journal of Geophysical Research* **6**, 2071–88.

Duan FH, Li YJ, Zhi Q, Yang GX and Gao JB (2019) Petrogenesis and geodynamic implications of Late Carboniferous sanukitic dikes from the Bieluagaxi area of West Junggar, NW China. *Journal of Asian Earth Science* **175**, 158–77.

Duggen S, Hoernle K, Van den Bogaard P and Garbe-Schonberg D (2005) Post-collisional transition from subduction- to intraplate-type magmatism in the westernmost Mediterranean: evidence for continental-edge delamination of subcontinental lithosphere. *Journal of Petrology* **46**, 1155–201.

Fan JJ, Wang Q, Li J, Wei GJ, Wyman D, Zhao ZH, Liu Y, Ma JL, Zhang L and Wang ZL (2020) Molybdenum and Boron isotopic compositions of porphyry Cu mineralization-related adakitic rocks in Central-Eastern China: new insights into their petrogenesis. *Journal of Geophysical Research: Solid Earth* **125**, e2020JB020474.

Feng YM, Coleman RG, Tilton G and Xiao XC (1989) Tectonic evolution of the west Junggar region, Xinjiang, China. *Tectonics* **8**, 729–52.

Ferry JM and Watson EB (2007) New thermodynamic models and revised calibrations for the Ti-in-zircon and Zr-in-rutile thermometers. *Contributions to Mineralogy and Petrology* **154**, 429–37.

Furukawa Y and Tatsumi Y (1999) Melting of a subducting slab and production of high-Mg andesite magmas: unusual magmatism in SW Japan. *Geophysical Research Letters* **26**, 2271–4.

Gao R, Xiao L, Pirajno F, Wang GC, He XX, Yang G and Yan SW (2014) Carboniferous-Permian extensive magmatism in the West Junggar, Xinjiang, northwestern China: its geochemistry, geochronology, and petrogenesis. *Lithos* **204**, 125–43.

Ge XY, Li XH, Chen ZG and Li WP (2002) Geochemistry and petrogenesis of Jurassic high Sr/low Y granitoids in eastern China: constraints on crustal thickness. *Chinese Science Bulletin* **47**, 474–80 (in Chinese).

Geng HY, Sun M, Yuan C, Xiao WJ, Xian WS, Zhao GC, Zhang LF, Wong K and Wu FY (2009) Geochemical, Sr-Nd and zircon U-Pb-Hf isotopic studies of Late Carboniferous magmatism in the West Junggar, Xinjiang: implications for ridge subduction? *Chemical Geology* **266**, 364–89.

Geng HY, Sun M, Yuan C, Zhao GC and Xiao WJ (2011) Geochemical and geochronological study of Early Carboniferous volcanic rocks from the West Junggar: petrogenesis and tectonic implications. *Journal of Asian Earth Sciences* **42**, 854–66.

Guo F, Nakamuru E, Fan WM, Kobayoshi K and Li CW (2007) Generation of Palaeocene adakitic andesites by magma mixing; Yanji area, NE China. *Journal of Petrology* **48**, 661–92.

Gill JB (1981) *Orogenic andesites and plate tectonics. Minerals and Rocks.* Berlin, Heidelberg, New York: Springer-Verlag.

Green TH and Pearson NJ (1986) Rare-earth element partitioning between titanite and coexisting silicate liquid at high pressure and temperature. *Chemical Geology* **55**, 105–19.

Grimes CB, John BE, Kelemen PB, Mazdab FK, Wooden JL, Cheadle MJ, Hanghoj K and Schwartz JJ (2007) Trace element chemistry of zircons from oceanic crust; a method for distinguishing detrital zircon provenance. *Geology* **35**, 643–6.

Han BF, Ji JQ, Song B, Chen LH and Zhang L (2006) Late Paleozoic vertical growth of continental crust around the Junggar Basin, Xinjiang, China (Part I): timing of post-collisional plutonism. *Acta Petrologica Sinica* **22**, 1077–86 (in Chinese with English abstract).

Han YG and Zhao GC (2018) Final amalgamation of the Tianshan and Junggar orogenic collage in the southwestern central Asian orogenic belt: constraints on the closure of the Paleo-Asian Ocean. *Earth Science Reviews* **186**, 129–52.

He GQ, Liu JB, Zhang YQ and Xu X (2007) Karamay ophioliic mélange formed during Early Paleozoic in western Junggar basin. *Acta Petrologica Sinica* **23**, 1573–6 (in Chinese with English abstract).

He Q, Xiao L, Wei QR and Ni PZ (2009) Petrological and geochemical characteristics of the Jiyidu ophiolitic mélange, West Yunnan: Constraints for its tectonic implications. *Acta Petrologica Sinica* **25**, 3229–40 (in Chinese with English abstract).

He XX (2012) Petrogenesis and geological implications of Late Paleozoic intermediate-basic dyke swarms in western Junggar. MSc Dissertation. China University of Geosciences, Wuhan, 1–58.

He XX, Xiao L, Wang GC, Gao R, Yang G and Yan SW (2015) Petrogenesis and geological implications of Late Paleozoic intermediate-basic dyke swarms in western Junggar. *Earth Science-Journal of China University of Geosciences* **40**, 777–96 (in Chinese with English abstract).

Hirose K (1997) Melting experiments on Iherzoilite KLB-1under hydrous conditions and generation of high-magnesium andesitic melts. *Geology* **25**, 42–4.

Hou GT (2012) Mechanism for three types of mafic dykes swarms. *Geoscience Frontiers* **3**, 217–23.

Hu AQ, Jahn BM, Zhang GX, Chen YB and Zhang QF (2000) Crustal evolution and Phanerozoic crustal growth in northern Xinjiang: Nd isotopic evidence. Part I. Isotopic characterization of basement rocks. *Tectonophysics* **328**, 15–51.

Jahn BM, Capdevila R, Liu DY, Vernon A and Badarch G (2004) Sources of Phanerozoic granitoids in the transect Bayanhongor-Ulaan Baatar, Mongolia: geochemical and Nd isotopic evidence, and implications for Phanerozoic crustal growth. *Journal of Asian Earth Sciences* **23**, 629–53.

Jahn BM, Wu FY and Chen B (2000) Massive graitoids generation in Central Asia: Nd isotope evidence and implication for continental growth in the Phanerozoic. *Episodes* **23**, 82–92.

Johnson MC and Plank T (1999) Dehydration and melting experiments constrain the fate of subducted sediments. *Geochemistry Geophysics Geosystem* **1**, 1007.

Kamei A, Owada M, Nagao T and Shiraki K (2004) High-Mg diorites derived from sanukitic HMA magmas, Kyushu Island, southwest Japan arc: evidence from clinopyroxene and whole rock compositions. *Lithos* **75**, 359–71.

Kelemen PB (1995) Genesis of high Mg andesites and the continental crust. *Contributions to Mineralogy and Petrology* **120**, 1–19.

Kelemen PB, Yogodzinski GM and Scholl DW (2003) Along-strike variation in the Aleutian Island arc: genesis of High Mg# Andesite and Implications for Continental Crust. *Geophysical Monograph Series* **138**, 223–76.

Li D, He DF and Fan C (2015) Geochronology and Sr-Nd-Hf isotopic composition of the granites, enclaves, and dikes in the Karamay area, NW China: insights into late Carboniferous crustal growth of West Junggar. *Geoscience Frontiers* **6**, 153–73.

Li JW, Zhao XF, Zhou MF, Ma CQ, Souza ZS and Vasconcelos P (2009) Late Mesozoic magmatism from the Daye region, eastern China: U–Pb ages, petrogenesis, and geodynamic implications. *Contributions to Mineralogy and Petrology* **157**, 383–409.

Li XH, Li ZX, Li WX, Wang XC and Gao YY (2013) Revisiting the "C-type adakites" of the Lower Yangtze River Belt, central eastern China: In-situ zircon Hf–O isotope and geochemical constraints. *Chemical Geology* **345**, 1–15.

Li XZ, Han BF, Li ZH, Liu ZQ and Du W (2005) Mechanism of the Karamay basic-intermediate dyke swarm from Xinjiang and tectonic implications. *Geological Review* **51**, 517–22 (in Chinese with English abstract).

Liu B, Han, BF, Chen JF, Ren R, Zheng B, Wang ZZ and Feng LX (2017) Closure time of the Junggar-Balkhash ocean: constraints from late Paleozoic volcanosedimentary sequences in the Barleik mountains, West Junggar, NW China. *Tectonics* **36**, 2823–45.

Liu B, Han BF, Xu Z, Ren R and Chen JF (2019) The Ediacaran to Early Palaeozoic evolution of the Junggar-Balkhash Ocean: a synthesis of the ophiolitic melanges in the southern West Junggar terrasne, NW China. *Geological Journal* **55**, 1689–707.

Liu B, Ma CQ, Tang YJ, Dong H, Xu Y, Zhao SQ, Sun Y and Huang J (2021) Triassic high-Mg andesitic magmatism induced by sediment melt-peridotite interactions in the central Tibetan Plateau. *Lithos* **398–399**, 106266.

Liu XJ, Xu JF, Castillo PR, Xiao WJ, Shi Y, Feng ZH and Guo L (2014) The Dupal isotopic anomaly in the southern Paleo-Asian Ocean: Nd–Pb isotope evidence from ophiolites in Northwest China. *Lithos* **189**, 185–200.

Ma C, Xiao WJ, Windley BF, Zhao GP, Han CM, Zhang JE, Luo J and Li C (2012) Tracing a subducted ridge-transform system in a late Carboniferous accretionary prism of the southern Altaids: orthogonal sanukitoid dyke swarms in Western Junggar, NW China. *Lithos* **140–141**, 152–65.

Ma FZ, Chen XH, Xu SL, Ma F, Han LL, Ding WC and Wang Y (2020) LA-ICP-MS zircon U-Pb dating and geochemistry of the Late Paleozoic sanukitoids in the Hongshan area, west Junggar. *Acta Petrologica Sinica* **94**, 1462–81 (in Chinese with English abstract).

Mahood G and Hildreth W (1983) Large partition coefficients for trace elements in high silica rhyolites. *Geochimica et Cosmochimica Acta* **47**, 11–30.

Martin H, Smithies RH, Rapp R, Moyen JF and Champion D (2005) An overview of adakite, tonalite–trondhjemite–granodiorite (TTG), and sanukitoid: relationships and some implications for crustal evolution. *Lithos* **79**, 1–24.

Martinez-Poza AI and Druguet E (2016) Structure and tectonic setting of the SE Sardinia mafic swarm: Insights for the stress state during magma emplacement in the upper crust. *Journal of Geodynamics* **101**, 170–85.

McCarron JJ and Smellie JL (1998) Tectonic implications of fore-arc magmatism and generation of high-magnesium andesites: Alexander island, Antarctica. *Journal of the Geological Society* **155**, 269–80.

Mukasa SB, Blatter DL and Andronikov AV (2007) Mantle peridotite xenolith in andesite lava at El Penon, central Mexican Volcanic Blet: isotopic and trace element evidence for melting and metasomatism in the mantle wedge beneath an active arc. *Earth and Planetary Science Letters* **260**, 37–55.

Nowell GM, Kempton PD, Noble SR, Fitton JG, Saunders AD, Mahoney JJ and Taylor RN (1998) High precision Hf isotope measurements of MORB and OIB by thermal ionisation mass spectrometry: insights into the depleted mantle. *Chemical Geology* **149**, 211–33.

Patchett PJ and Samson SD (2003) Ages and growth of the continental crust from radiogenic isotopes. *Treatise on Geochemistry* **3**, 321–48.

Paterson SR, Vernon RH and Tobisch OT (1989) A review of criteria for the identification of magmatic and tectonic foliations in granitoids. *Journal of Structural Geology* **11**, 349–63.

Pearce JA (1982) *Trace Element Characteristics of Lavas from Destructive Plate Margins. Orogenic Andesites and Related Rocks*. New York, Andesites: Wiley, pp.524–48.

Pearce JA, Harris NBW and Tindle AG (1984) Trace element discrimination diagrams for the tectonic interpretation of granitic rocks. *Journal of Petrology* **25**, 956–83.

Plank T (2005) Constraints from Thorium/Lanthanum on sediment recycling at subduction zones and the evolution of the continents. *Journal of Petrology* **46**, 921–44.

Plank T, Kelley KA, Murray RW and Stern LQ (2007) Chemical composition of sediments subducting at the Izu-Bonin trench. *Geochemistry Geophysics Geosystem* **8**, Q04l16.

Plank T and Langmuir CH (1998) The chemical composition of subducting sediment and its consequences for the crust and mantle. *Chemical Geology* **145**, 325–94.

Qian Q and Hermann J (2010) Formation of high-Mg diorites through assimilation of peridotite by monzodiorite magma at crustal depths. *Journal of Petrology* **51**, 1381–16.

Rapp RP, Shimizu N, Norman MD and Applegate GS (1999) Reaction between slab-derived melts and peridotite in the mantle wedge: experimental constraints at 3.8 GPa. *Chemical Geology* **160**, 335–56.

Rapp RP and Watson EB (1995) Dehydration melting of metabasalt at 8–32 kbar: implications for continental growth and crust-mantle recycling. *Journal of Petrology* **36**, 891–931.

Ren R (2013) Paleozoic magmatism and intra-oceanic subduction-accretion process in the southern part of West Junggar, Xinjiang. PhD Dissertation. Peking University, 84–8.

Rollinson HR (1993) *Using Geochemical Data: Evaluation, Presentation, Interpretation*. London: Longman Scientific & Technical, pp. 1–352.

Rudnick RL and Gao S (2003) Composition of the continental crust. *Treatise on Geochemistry* **3**, 1–64.

Schiano P, Monzier M, Eissen JP, Martin H and Koga KT (2010) Simple mixing as the major control of the evolution of volcanic suites in the Ecuadorian Andes. *Contributions to Mineralogy and Petrology* **160**, 297–312.

Sengor AMC, Natalin BA and Burtman VS (1993) Evolution of the Altaid tectonic collage and crustal growth in Eurasia. *Nature* **364**, 299–307.

Shimoda G, Tatsumi Y, Nohda S, Ishizaka K and Jahn BM (1998) Setouchi high-Mg andesites revisited: geochemical evidence for melting of subducted sediments. *Earth and Planetary Science Letters* **160**, 479–92.

Su Y and Langmuir CH (2003) Global MORB chemistry compilation at the segment scale, PhD Thesis, Department of Earth and Environmental Sciences, Columbia University.

Sun SS and McDonough WF (1989) Chemical and isotopic systematics of oceanic basalts: implications for mantle composition and processes. In: Saunders A D, Nonrry MJ Magmatism in the Oceanic Basins. *Geological Society, London, Special Publications* **42**, 313–45.

Tang GJ, Wang Q, Wyman DA, Li ZX, Zhao ZH, Jia XH and Jiang ZQ (2010) Ridge subduction and crustal growth in the Central Asian Orogenic Belt: evidence from Late Carboniferous adakites and high-Mg diorites in the western Junggar region, northern Xinjiang (west China). *Chemical Geology* **277**, 281–300.

Tang GJ, Wang Q, Wyman DA, Li ZX, Xu YG and Zhao ZH (2012a) Recycling oceanic crust for continental crustal growth: Sr-Nd-Hf isotope evidence from granitoids in the western Junggar region, NW China. *Lithos* **128–131**, 73–83.

Tang GJ, Wang Q, Wyman DA, Li ZX, Zhao ZH and Yang YH (2012b) Late Carboniferous high εNd(t)-εHf(t) granitoids, enclaves and Dykes in western Junggar, NW China: ridge-subduction-related magmatism and crustal growth. *Lithos* **140–141**, 86–102.

Tang GJ, Wyman DA, Wang Q, Li J, Li ZX, Zhao ZH and Sun WD (2012c) Asthenosphere-lithosphere interaction triggered by a slab window during ridge subduction: trace element and Sr-Nd-Hf-Os isotopic evidence from Late Carboniferous tholeiites in the western Junggar area (NW China). *Earth and Planetary Sciences Letters* **329**, 84–96.

Tatsumi Y (2006) High-Mg andesites in the Setouchi volcanic belt, southwestern Japan: analogy to Archean magmatism and continental crust formation? *Annual Review of Earth and Planetary Sciences* **34**, 467–99.

Tatsumi Y (2008) Making continental crust: the Sanukitoid connection. *Chinese Science Bulletin* **53**, 978–90.

Tatsumi Y (2001) Geochemical modeling of partial melting of subducting sediments and subsequent melt–mantle interaction: generation of high-Mg andesites in the Setouehi volcanic belt, Southwest Japan. *Geology* **29**, 323–6.

Tatsumi Y and Hanyu T (2003) Geochemical modeling of dehydration and partial melting of subducting lithosphere: toward a comprehensive understanding of high-Mg andesite formation in the Setouchi volcanic belt, SW Japan. *Geochemistry Geophysics Geosystems* **4**, 1081.

Tatsumi Y, Shukuno H, Sato K, Shibata T and Yoshikawa M (2003) The petrology and geochemistry of high-magnesium andesites at the western tip of the Setouchi volcanic belt, SW Japan. *Journal of Petrology* **44**, 1561–78.

Tian Y and Shan YH (2011) The diversity of flow structures in felsic dykes. *Journal of Geological Society* **168**, 1001–11.

Treuil M and Joron JL (1975) Utilization des ~16ments hygromagmatophiles pour la simplification de la modelisation quantitative des processus magmatiques, exemples de I' Afar et de la dorsale m~dio~atlantiques. *Rendiconti Societa Ititaliana Mineralogia Petrografia* **31**, 125–74.

Vervoort JD, Plank T and Prytulak J (2011) The Hf–Nd isotopic composition of marine sediments. *Geochimica et Cosmochimica Acta* **75**, 5903–26.

Wang CG, Cascio ML, Liang Y and Xu WL (2020) An experimental study of peridotite dissolution in eclogite-derived melts: implications for styles of melt-rock interaction in lithospheric mantle beneath the North China Craton. *Geochimica et Cosmochimica Acta* **278**, 157–76.

Wang Q, Li ZX, Chung SL, Wyman DA, Sun YL, Zhao Z, Zhu Y and Qiu H (2011) Late Triassic high-Mg andesite/dacite suites from northern Hohxil, North Tibet: geochronology, geochemical characteristics, petrogenetic processes and tectonic implications. *Lithos* **126**, 54–67.

Wang Q, Xu JF, Jian P, Bao ZW, Zhao ZH, Li CF, Xiong XL and Ma JL (2006) Petrogenesis of adakitic porphyries in an extensional tectonic setting, Dexing, South China: implications for the genesis of porphyry copper mineralization. *Journal of Petrology* **47**, 119–44.

Whalen JB, Currie KL and Chappell BW (1987) A-type granites: geochemical characteristics, discrimination and petrogenesis. *Contributions to Mineralogy and Petrology* **95**, 407–19.

Whalen JB, McNicoll VJ, van Staal CR, Lissenberg CJ, Longstaffe FJ, Jenner GA and van Breeman O (2006) Spatial, temporal and geochemical characteristics of Silurian collision-zone magmatism, Newfoundland Appalachians: an example of a rapidly evolving magmatic system related to slab break-off. *Lithos* **89**, 377–404.

Wilde SA, Wu FY and Zhao GC (2010) The Khanka Block, NE China and its significance for the evolution of the Central Asian Orogenic Belt and continental accretion. *Geological Society of London, Special Publication* **338**, 117–37.

Windley BF, Alexeiev D, Xiao WJ, Kroner A and Badarch G (2007) Tectonic models for accretion of the Central Asian Orogenic Belt. *Journal of the Geological Society* **164**, 31–47.

Windley BF and Xiao WJ (2018) Ridge subduction and slab windows in the Central Asian Orogenic Belt: tectonic implications for the evolution of an accretionary orogen. *Gondwana Research* **61**, 73–87.

Woodhead JD, Hergt JM, Davidson JP and Eggins SM (2001) Hafnium isotope evidence for conservation element mobility during subduction zone processes. *Earth and Planetary Science Letters* **192**, 331–46.

Woodland AB, Bulatov VK, Brey GP, Girnis AV, Höfer HE and Gerdes A (2018) Subduction factory in an ampoule: experiments on sediment–peridotite interaction under temperature gradient conditions. *Geochimica et Cosmochimica Acta* **223**, 319–49.

Workman RK and Hart SR (2005) Major and trace element composition of the depleted MORB mantle (DMM). *Earth Planetary Science Letters* **231**, 53–72.

Wu FY, Ge WC and Sun DY (2002) The definition, discrimination of adakites and their geological role. In *The Ways of Investigation on Granitoids* (eds. QH Xiao, JF Deng, DQ Ma, *et al.*), pp. 172–91. Beijing: Geological Publishing House (in Chinese with English abstract).

Wu SC, Yang YJ, Xu YX, Afonso JC and Zhang AQ (2023) A fossil oceanic lithosphere preserved inside a continent. *Geology* **51**, 204–8.

Wu YB and Zheng YF (2004) Genesis of zircon and its constraints on interpretation of U–Pb age. *Chinese Science Bulletin* **49**, 1589–604.

Xiao WJ, Han CM, Yuan C, Sun M and Lin SF (2008) Middle Cambrian to Permian subduction-related accretionary orogenesis of Northern Xinjiang, NW China: implications for the tectonic evolution of Central Asia. *Journal of Asian Earth Sciences* **33**, 102–17.

Xiao WJ, Huang BC, Han CM, Sun S and Li JL (2010) A review of the western part of the Altaids: a key to understanding the architecture of accretionary orogens. *Gondwana Research* **18**, 253–73.

Xiao WJ and Santosh M (2014) The western Central Asian Orogenic Belt: a window to accretionary orogenesis and continental growth. *Gondwana Research* **25**, 1429–44.

Xiong XL (2006) Trace element evidence for growth of early continental crust by melting of rutile-bearing hydrous eclogite. *Geology* **34**, 945–8.

Xiong XL, Cai ZY, Niu HC, Chen YB, Wang Q, Zhao ZH and Wu JH (2005) The late Paleozoic adakites in eastern Tianshan area and their metallogenetic significance. *Acta Petrologica Sinica* **21**, 967–76 (in Chinese with English abstract).

Xu QQ, Ji JQ, Zhao L, Gong JF, Zhou J, He GQ, Zhong DL, Wang GJ and Griffiths L (2013) Tectonic evolution and continental crust growth of Northern Xinjiang in northwestern China: Remant ocean model. *Earth Science Reviews* **126**, 178–205.

Xu X, He GQ, Li HQ, Ding TF, Liu XY and Mei SW (2006) Basic characteristics of the Karamay ophiolitic melange, Xinjiang, and its zircon SHRIMP dating. *Geology in China* **33**, 470–5 (in Chinese with English abstract).

Yang GX, Li YJ, Gu PY, Yang BK, Tong L and Zhang HW (2012a) Geochronological and geochemical study of the Darbut Ophiolitic Complex in the West Junggar (NW China): implications for petrogenesis and tectonic evolution. *Gondwana Research* **21**, 1037–49.

Yang GX, Li YJ, Santosh M, Gu PY, Yang BK, Zhang B, Wang HB, Zhong X and Tong L (2012b) A Neoproterozoic seamount in the Pa;eoasian Ocean: evidences from zircon U-Pb geochronology and geochemistry of the Mayile ophiolitic melange in West Junggar, NW China. *Lithos* **140–141**, 53–65.

Yang GX, Li YJ, Santosh M, Yang BK, Zhang B and Tong L (2013) Geochronology and geochemistry of basalts from the Karamay ophiolitic melange in West Junggar (NW China): implications for Devonian-Carboniferous intra-oceanic accretionary tectonics of the southern Altaids. *Geological Society of America Bulletin* **125**, 401–19.

Yin JY, Chen W, Xiao WJ, Yuan C, Sun M, Tang GJ, Yu S, Long XP, Cai KD, Geng HY, Zhang Y and Liu XY (2015a) Petrogenesis of Early-Permian sanukitoids from West Junggar, Northwest China: implications for Late Paleozoic crustal growth in Central Asia. *Tectonophysics* **662**, 385–97.

Yin JY, Chen W, Yuan C, Yu S, Xiao WJ, Li J and Sun JB (2015b) Petrogenesis of Early Carboniferous adakitic Dykes, Sawuer region, northern West Junggar, NW China: implications for geodynamic evolution. *Gondwana Research* **27**, 1630–45.

Yin JY, Long XP, Yuan C, Sun M, Zhao GC and Geng HY (2013) A Late Carboniferous slab window: geochronological and geochemical evidence from mafic to intermediate dykes in West Junggar, NW China. *Lithos* **175–176**, 146–62.

Yin JY, Yuan C, Sun M, Long XP, Qiu HN, Wang YJ, Ren JB and Guan YL (2012) Age, geochemical features and possible petrogenesis mechanism of Early Permian magnesian diorite in Hatu, Xinjiang. *Acta Petrologica Sinica* **28**, 2171–82.

Yin JY, Yuan C, Sun M, Long XP, Zhao GC, Wong KP, Geng HY and Cai K (2010) Late Carboniferous high-Mg dioritic Dykes in Western Junggar, NW China: geochemical features, petrogenesis and tectonic implications. *Gondwana Research* **17**, 145–52.

Yurimoto H, Duke EF, Papike JJ and Shearer CK (1990) Are discontinuous chondritenormalized REE patterns in pegmatitic granite systems the results of monazite fractionation? *Geochimica et Cosmochimica Acta* **54**, 2141–5.

Zhan Y, Hou GT, Hari KR and Shu WL (2015) Geochemical and isotopic constraints on the evolution of Late Paleozoic dyke swarms in West Junggar, Xinjiang, China. *Journal of Asian Earth Science* **113**, 126–36.

Zhang CL and Zou HB (2013) Comparison between the Permian mafic dykes in Tarim and the western part of Central Orogenic Belt (CAOB), NW China: implications for two mantle domains of the Permian Tarim Large Igneous Province. *Lithos* **174**, 15–27.

Zhang JE, Xiao WJ, Han CM, Ao SJ, Yuan C, Sun M, Geng HY, Zhao GC, Guo QQ and Ma C (2011a) Kinematics and age constraints of deformation in a Late Carboniferous accretionary complex in Western Junggar, NW China. *Gondwana Research* **19**, 958–74.

Zhang JE, Xiao WJ, Han CM, Mao QG, Ao SJ, Guo QQ and Ma C (2011b) A Devonian to Carboniferous intra-oceanic subduction system in Western Junggar, NW China. *Lithos* **125**, 592–606.

Zhang P, Wang GC, Polat A, Zhu CY, Shen TY, Chen Y, Chen C, Guo JS, Wu GL and Liu YT (2018) Emplacement of the ophiolitic melanges in the west Karamay area: implications for the Late Paleozoic tectonic evolution of West Junggar, northwestern China. *Tectonophysics* **747–748**, 259–80.

Zhang P, Wang GC, Shen TY, Polat A and Zhu CY (2021a) Paleozoic convergence processes in the southwestern Central Asian Orogenic Belt: insights from U-Pb dating of detrital zircons from West Junggar, northwestern China. *Geoscience Frontiers* **12**, 531–48.

Zhang XR, Zhao GC Sun M, Eizenh€ofer PR, Han YG, Hou WZ, Liu DX, Wang B, Liu Q and Xu B (2016) Tectonic evolution from subduction to arc-continent collision of the Junggar Ocean: constraints from U-Pb dating and Hf isotopes of detrital zircons from the North Tianshan belt, NW China. *Geological Society of America Bulletin* **128**, 644–60.

Zhang ZG, Liu XJ, Xiao WJ, Xu JF, Shi Y, Gong XH, Hu RG, Liu PD, Song YJ, Xiao Y, Zhang ZQ Li R and Li DC (2021b) Geochemistry and Sr-Nd-Hf-Pb isotope systematics of late Carboniferous sanukitoids in northern West JUnggar, NW China: implications for initiation of ridge-subduction. *Gondwana Research* **99**, 204–18.

Zhao JM, Huang Y, Ma ZJ, Shao XZ, Cheng HG, Wang W and Xu Q (2008) Discussion on the basement structure and property of northern Junggar basin. *Chinese Journal of Geophysics* **51**, 1767–75 (in Chinese with English abstract).

Zheng B, Han BF, Wang ZZ, Liu B and Feng LX (2020) An example pf Ohanerozoic continental crustal growth: the West Junggar Orogenic Belt, Northwest China. *Lithos* **376–377**, 105745.

Zheng JP, Sun M, Zhao GC, Robinson P and Wang FZ (2007) Elemental and Sr-Nd-Pb isotopic geochemistry of Late Paleozoic volcanic rocks beneath the Junggar basin, NW China: implications for the formation and evolution of the basin basement. *Journal of Asian Earth Sciences* **29**, 778–94.

Zhou LY and Wang Y (2012) Late Carboniferous syn-tectonic magmatic flow at the northern margin of the North China Craton – evidence for the reactivation of the cratonic basement. *Journal of Asian Earth Sciences* **54–55**, 131–42.

Zhu YF, Chen B and Qiu T (2015) Geology and geochemistry of the Baijiantan – Baikouquan ophiolitic melanges: implications for geological evolution of west Junggar, Xinjiang, NW China. *Geological Magazine* **152**, 41–69.

Zong RW, Wang ZZ, Jiang T and Gong YM (2016) Late Devonian radiolarian-bearing siliceous rocks from the Karamay ophiolitic melange in western Junggar: implications for the evolution of the Paleo-Asian Ocean. *Palaeogeography, Palaeoclimatology, Palaeoecology* **448**, 266–78.